

# **MODELLING OF WIND DIRECTION SIGNALS IN POLARIMETRIC SEA SURFACE BRIGHTNESS TEMPERATURES**

**Simon H. Yueh**

**Jet Propulsion Laboratory  
California Institute of Technology  
4800 Oak Grove Drive  
Pasadena, CA 91109  
Tel: (818) 354-3012, Fax: (818) 393-5285**

**Submitted to IEEE Transactions on (geoscience and Remote Sensing**

**October 19, 1995**

## Abstract

There has been an increasing interest in the applications of polarimetric microwave radiometers for ocean wind remote sensing. Aircraft and spaceborne radiometers have found significant wind direction signals in sea surface brightness temperatures, in addition to their sensitivities on wind speeds. However, it is not yet understood what physical scattering mechanisms produce the observed wind direction dependence. To this end, polarimetric microwave emissions from wind-generated sea surfaces are investigated with a polarimetric two-scale scattering model of sea surfaces, which relates the directional wind-wave spectrum to passive microwave signatures of sea surfaces. Theoretical azimuthal modulations are found to agree well with experimental observations for all Stokes parameters from near nadir to  $65^\circ$  incidence angles. The up/downwind asymmetries of brightness temperatures are interpreted using the hydrodynamic modulation. The contributions of Bragg scattering by short waves, geometric optics scattering by long waves and sea foam are examined. The geometric optics scattering mechanism underestimates the directional signals in the first three Stokes parameters, and most importantly it predicts no signals in the fourth Stokes parameter ( $V$ ), in disagreement with experimental data. In contrast, the Bragg scattering contributes to most of the wind direction signals from the two-scale model and correctly predicts the phase changes of the up/crosswind asymmetries in  $T_v$  and  $U$  from middle to high incidence angles. The accuracy of the Bragg scattering theory for radiometric emission from water ripples is corroborated by the numerical Monte Carlo simulation of rough surface scattering. This theoretical interpretation indicates the potential use of polarimetric brightness temperatures for retrieving the directional wave spectrum of capillary waves.

# 1 Introduction

Sea surface brightness temperatures are the radiometric power measure of blackbody radiation from sea water. The blackbody radiation is the electromagnetic waves excited by the random thermal motion of charged particles in the sea water. While the emitted electromagnetic waves transmitting through the air-water interface, the water waves present on the surface and marine mixed layers will scatter the electromagnetic waves into the atmosphere. Through this electromagnetic-water wave interaction process, the signatures of atmospheric and oceanic characteristics are embedded in the sea surface brightness temperatures measured with passive radiometers. Experimental results, such as those published in [1, 2], have shown the correlation of sea surface brightness temperatures with the near surface wind velocity.

Wind is the key driving force in air-sea interaction processes, creating the momentum transfer between the atmosphere and ocean and generating the large scale ocean circulations and surface waves. Wind-roughened surfaces in the form of gravity and capillary waves, breaking waves and foam, are the result of the balance of the wind input and dissipative processes, including viscous dissipation and wave breaking. Due to a preferential direction of wind forcing, the surface waves are skewed with a rougher surface profile along the wind direction. This can be characterized by a larger root-mean-square (rms) surface slope and height along the wind direction than those across. Additionally, there are couplings between capillary waves and gravity waves with a longer wavelength denoted as carrier waves. This wind-wave interaction causes the leeward face of the carrier waves to have more capillary ripples than the windward face. Over a critical wind velocity, depending on the air-sea temperature difference and water salinity, waves may become unstable and break with forward plunging to dissipate the energy provided by the wind. As the air bubbles entrained in water by the breaking waves gradually rising to the surface, foaming whitecaps consisting of mixed air bubbles with water are present on the surface.

These wind-generated surface features affect the sea surface brightness temperatures

through three primary scattering mechanisms. First is the Bragg scattering by capillary waves, which are known to be significant scattering sources for scatterometry [3], Second is the tilting effects caused by large-scale waves, with wavelength longer than those of capillary waves contributing to Bragg scattering. Third is caused by whitecaps or foam, which significantly enhances the albedo of the sea surface. The rms height of capillary waves, rms slope of long waves, and coverage of foam on sea surfaces are all functions of surface wind velocity. Other less well studied scattering sources include the breaking waves and wedges before breaking, which are believed to be important scattering sources for scatterometry at large incidence angles.

The Bragg scattering mechanism exhibited in radiometry differs from that in scatterometry. The Bragg scattering contributes to the brightness temperatures through a “bistatic” scattering mechanism, unlike the “monostatic” scattering measurements by scatterometers. In the context of electromagnetic wave interaction with the capillary wavenumber spectrum, radiometer signals are the integral effects of Bragg scattering over a range of capillary wavenumbers [4], while scatterometers sample the wave spectrum at a single point. Despite the described difference, the Bragg scattering from capillary waves modifying the surface reflectivities, influences the thermal radiation and backscattering from sea surfaces at all incidence angles.

The scattering effects of large-scale waves have been modeled by the geometric optics (GO) scattering theory [5, 22]. In the GO model, the large-scale waves are modeled by tilting surface facets, and the scattering coefficients are proportional to the number of surface facets with a tilting angle satisfying the specular reflection condition. Stogryn [5] used Cox and Munk’s slope distribution of sea surfaces [6] obtained from the sun’s glitter measurements and studied the sensitivity of brightness temperatures on wind speed. However, Hollinger’s tower measurements [1] performed at 1, 8 and 19 GHz showed that the GO model failed to account for the observational frequency dependence and significantly underestimated the wind speed dependence of the horizontal component at small incidence angles. This discrepancy was

due to the neglect by Stogryn's model of small-scale surface roughness, which contribute to the Bragg scattering of incident electromagnetic waves.

With the Bragg scattering mechanism taken into consideration, the two-scale scattering theory [7] was extended by Wu and Fung [8] and Wentz [9] to interpret the brightness temperatures of sea surfaces. In the two-scale scattering approach, the reflection coefficients of large-scale waves are reduced by the scattering effects of short-scale waves and the Bragg scattering from the short-scale waves are averaged over the slopes of long waves. Improved agreement with measured scattering and emission coefficients was demonstrated. However, the rms height of the short waves used in Wu and Fung's model was selected by fitting theory to experimental data. To avoid an ad-hoc selection of spectrum parameters, Wentz's two-scale model used an empirical sea spectrum [10]. As compared with the geometric optics model, the two-scale theory more accurately modeled the dependence of brightness temperatures on incidence angles and wind velocities.

Besides the wind speed sensitivity, capillary waves, gravity waves, and foam are anisotropic in azimuth direction due to the preferential direction of wind forcing. These surface asymmetries cause ocean backscatters to vary with the wind direction, and recently are found to induce the directional dependence of sea surface brightness temperatures in near-nadir measurements performed by the Russian scientists at the Space Research Institute [11], SSM/I's dual-polarization measurements at  $53^\circ$  incidence angle [12], and 19 and 37 GHz polarimetric measurements made by JPL's wind radiometer (WINDRAD) in the incidence angle range of  $30^\circ$  to  $65^\circ$  [14, 15]. In particular, the off-nadir measurements [14, 15] showed that there are up/downwind asymmetries in the azimuth dependence of sea surface brightness temperatures. Since brightness temperatures are influenced by surface scattering as discussed previously, it should not be surprising to find that passive radiometer measurements of the sea surface are sensitive to the wind direction.

However, it is not yet understood what scattering mechanisms produce the wind direction signals in the aforementioned passive microwave radiometer measurements. In Wu and

Fung's [8] and Wentz's [9] models, the surface spectrum of short waves were assumed to be isotropic and the Bragg scattering theory used was for isotropic surfaces. Consequently, there were no directional sensitivities in theoretical brightness temperatures. In contrast, Stogryn's geometric optics model using Cox and Munk's slope distribution, although in poor agreement with the wind speed sensitivity of sea surface brightness temperatures, did predict an azimuthal variation of a few Kelvins. A lack of theoretical interpretation leads to the questions of whether the observed wind direction signals can be explained by known scattering mechanisms, including Bragg scattering, geometric optics scattering and sea foam, and which one of the scattering mechanisms may dominate.

The purpose of this paper is to examine the applicability of a two-scale model to the wind direction signals in polarimetric sea surface brightness temperatures. This model [18, 31] extends the previous two-scale models [8, 9] to surfaces with anisotropic directional spectrum and predicts all four Stokes parameters of sea surface brightness temperatures. This allows us to examine the relative significance of geometric tilting effects of long waves, Bragg scattering by short waves, the excess emission from sea foam and the hydrodynamic modulations of short-scale waves by long waves.

In Section 2, the theory of polarimetric radiometry is summarized. Section 3 presents a two-scale model for thermal emission from anisotropic wind waves and foam, Section 4 presents comparison of theoretical results and existing microwave brightness temperatures of sea surfaces. Section 5 illustrates the relative contributions of Bragg scattering, geometric optics scattering and sea foam. Numerical Monte Carlo scattering was performed to validate the accuracy of the second-order small perturbation method (SPM) used in the Bragg scattering model, Section 6 summarizes the results of this paper and discusses the issues required for further investigation.

## 2 Polarimetric Radiometry

The electromagnetic waves emitted from natural media due to random thermal motion of electric charges are in general partially polarized. To fully characterize the polarization state of partially polarized thermal radiation, four parameters  $I, Q, U$ , and  $V$  were introduced by Sir George Stokes. Because conventional radiometers for earth remote sensing pm-form  $T_v$  and  $T_h$  measurements, an alternate representation of the Stokes vector uses four parameters,  $T_v, T_h, U$ , and  $V$ ,

$$I_s = \begin{bmatrix} T_v \\ T_h \\ U \\ V \end{bmatrix} = c \begin{bmatrix} \langle |E_v|^2 \rangle \\ \langle |E_h|^2 \rangle \\ 2\text{Re} \langle E_v E_h^* \rangle \\ 2\text{Im} \langle E_v E_h^* \rangle \end{bmatrix} \quad (1)$$

$T_v$  and  $T_h$  are the brightness temperatures of vertical and horizontal polarizations, while  $U$  and  $V$  characterize the correlation between these two orthogonal polarizations. Note that the first two Stokes parameters are related to  $T_v$  and  $T_h$  by  $I(=T_v + T_h)$  representing the total radiated energy and  $Q(=T_v - T_h)$  the polarization balance. EC]. (1) defines the Stokes parameters in terms of the horizontally and vertically polarized components of electric fields ( $E_h$  and  $E_v$ ). The polarization vectors are related to the direction of propagation and are illustrated in Figure 1. The angular brackets denote the ensemble average of the argument, and  $c$  is a constant relating the brightness temperature to the electric energy density [32].

Recent interests in the applications of polarimetric radiometry for remote sensing started from the theoretical work [16, 17, 18], Ground-based experiments were carried out to investigate the Stokes parameters of thermal emission from periodic soil surfaces at X-band [19] and from sinusoidal water surfaces at Ku band [20], at X band [21], and at 94-GHz [22]. The surface profiles studied in these experiments were all one-dimensional with an rms height of a few centimeters, much rougher than the capillary waves in the open oceans. Hence, the measured brightness temperatures had an azimuthal variation of as large as 20 Kelvins, significantly larger than the measurements from ocean surfaces [11, 12, 14] and the theoretical predictions [18]. However, these results showed that the Stokes parameters of microwave radiation from surfaces with preferential directional features are functions of the azimuthal

viewing angles.

For wind-generated sea surfaces, the surface spectrum is symmetric with respect to the wind direction ( $\phi_w$ ) or the surfaces are statistically reflection symmetric with respect to  $\phi_w$  [23], if the effects of swell can be ignored. Denoting, the azimuthal observation angle of radiometer look direction by  $\phi_r$  and the relative azimuth angle by  $\phi = \phi_w - \phi_r$ . Yuch et al. [23] derived from Maxwell's equations using reflection symmetry that  $T_v$  and  $T_h$  are even functions of  $\phi$  and  $U$  and  $V$  are odd functions.

The even and odd symmetry properties allow us to expand the Stokes parameters in either cosine or sine series of the azimuth angle  $\phi$ . Hence, expanded to the second harmonic of  $\phi$ ,

$$T_v \simeq T_{v0} + T_{v1} \cos \phi + T_{v2} \cos 2\phi \quad (2)$$

$$T_h \simeq T_{h0} + T_{h1} \cos \phi + T_{h2} \cos 2\phi \quad (3)$$

$$U \simeq U_1 \sin \phi + U_2 \sin 2\phi \quad (4)$$

$$V \simeq V_1 \sin \phi + V_2 \sin 2\phi \quad (5)$$

The coefficients of first harmonics account for the up/downwind asymmetric surface features, while those of second harmonics for the up/crosswind asymmetry.

All coefficients are functions of oceanic, atmospheric, and some instrument parameters, including near surface wind velocity, swell, salinity, air and sea surface temperatures, incidence angle, polarization and frequency. The dominant geophysical parameter is the surface wind velocity according to the past experience of scatterometer measurements. However, other variables which may influence the wind stress or friction velocity, could become significant at low to moderate wind speeds. Understanding how these harmonic coefficients are related to these geophysical parameters is crucial to the use of these Stokes parameter measurements for the inversion of geophysical parameters.



### 3 Polarimetric 2-scale sea surface emission model

Two-scale sea surface models approximate the sea surface as a two-scale surface with short-scale ripples or capillary waves riding on the top of large-scale surfaces. With this picture, the total thermal emission from the surface is the sum of emissions from individual, slightly perturbed surface patches tilted by the underlying large-scale surface.

In this model, the Stokes vector of the thermal emission from a local surface patch is represented by  $I_{sl}$ . To account for the radiation from sea foam,  $I_{sl}$  is the sum of two terms, including the Stokes vector of the emission from foam-free, wind-roughened small-scale sea surfaces and that from the surface patches with 100 percent foam coverage, denoted by  $I_{ss}$  and  $I_{sf}$ , respectively. Hence,

$$I_{sl} = (1 - F_r)I_{ss} + F_r I_{sf} \quad (6)$$

with  $F_r$  representing the area percentage coverage of sea foam over sea surfaces,  $F_r$  is known to be a function of surface wind velocities as well as air and sea surface temperatures, and is calculated using the empirical sea foam fractional coverage algorithm [24] derived from the least square fit of experimental observations.

The Stokes vector of the two-scale surface is written as the average of  $I_{sl}$  over the slope distribution of large scale surface, denoted by  $P(S_x, S_y)$ . In addition to changing the local incidence and azimuth angles, the slope of the large scale surface affects the area of surface patch projected along the line of sight, meaning that the emission from smallscale surfaces has to be further weighted by the solid angle of the large-scale surface viewed by the radiometer. This results in the second factor inside the integral for the Stokes vector observed at the incidence angle  $\theta$  and azimuth angle  $\phi$ :

$$I_s = \int_{-\infty}^{\infty} dS'_y \int_{-\infty}^{\cot \theta} dS'_x I_{sl} (1 - \sin^2 \theta) P(S_x, S_y) \quad (7)$$

where

$$\begin{aligned} S_x &= S'_x \cos \phi - S'_y \sin \phi \\ S_y &= S'_x \sin \phi + S'_y \cos \phi \end{aligned} \quad (8)$$

In the above equations,  $S_x$  and  $S_y$  represent the surface slopes in  $x$  (upwind) and  $y$  (cross-wind) directions, while  $S'_x$  and  $S'_y$  represent the surface slopes along and across the radiometer azimuth observation direction, respectively. Integration over  $S'_x$  has to be limited to  $\cot \theta$  to account for the shadowing by the large-scale surfaces.

In the following subsections, we describe the empirical' surface spectrum used for the two-scale model and the formulas used to calculate the Stokes vectors of foam-free, small-scale sca surfaces and sca foam.

### 3.1 Two scale surface descriptions

In two-scale modeling approach, the surface spectra of large scale waves and small scale waves, denoted by  $W_l$  and  $W_s$ , respectively, are related to the sca surface spectrum  $W$  by

$$W_l(K, \phi_k) = \begin{cases} W'(K, \phi_k) & \text{if } K < k_d \\ 0 & \text{otherwise} \end{cases} \quad (9)$$

$$W_s(K, \phi_k) = \begin{cases} 0 & \text{if } K < k_d \\ W(K, \phi_k) & \text{otherwise} \end{cases} \quad (10)$$

The hydrodynamic modulation is introduced by modulating the spectrum of small scale waves by a coefficient  $h$  according to the local slope of large scale surfaces:

$$h = \begin{cases} 1.5 & \text{if } S_x/S_u < -1.25 \\ 1 - 0.4 S_x/S_u & \text{if } -1.25 \leq S_x/S_u \leq 1.25 \\ 0.5 & \text{if } 1.25 \leq S_x/S_u \end{cases} \quad (11)$$

This formula is chosen so that the ripples on the leeward side of long waves are enhanced, while those on the windward side are depressed.

The slope distribution function  $P(S_x, S_y)$  is assumed to be zero-mean Gaussian with the up and cross-wind slope variances, denoted by  $S_u^2$  and  $S_c^2$ , which are calculated from all surface spectral components with a wavenumber less than the two-scale cutoff  $k_d$ ,

$$S_u^2 = \int_0^\infty dK \int_0^{2\pi} d\phi_k K^3 \cos^2 \phi_k W_l(K, \phi_k) \quad (12)$$

$$S_c^2 = \int_0^\infty dK \int_0^{2\pi} d\phi_k K^3 \sin^2 \phi_k W_l(K, \phi_k) \quad (13)$$

### 3.2 Emission from Small-scale Waves

To extend two-scale models [8, 9] to anisotropic sea surfaces, the second-order perturbation solution of Bragg scattering from small-scale, anisotropic surfaces [4] is used to calculate  $I_{ss}$ . The energy conservation condition, crucial for calculating the brightness temperature using the Kirchhoff's law [25], was verified with the numerical Monte Carlo simulations of rough surface scattering [4].

The Stokes emission vector  $I_{ss}$  in the earth surface coordinate is related to that denoted by  $I'_{ss}$  in the local surface coordinate by the coordinate rotation shown in Appendix A. By using a polarimetric Kirchhoff's law [25, 32],  $I'_{ss}$  is related to the reflectivity vector ( $I_r$ ) of the small-scale sea surface by

$$I'_{ss} = T_s \begin{pmatrix} 1 \\ 1 \\ 0 \\ 0 \end{pmatrix} \quad \text{(IV)} \quad (14)$$

where  $T_s$  is the surface temperature.

Based on the second order solution of scattering from slightly perturbed rough surfaces [4],  $I_r$  is the sum of two terms,  $I_{rc}$  and  $I_{ri}$ :

$$I_r = I_{rc} + I_{ri} \quad (15)$$

$I_{ri}$  is the incoherent surface reflectivities, calculated by integrating incoherent polarimetric bistatic scattering coefficients  $\gamma_{\alpha\beta\mu\nu}^i$  over all incidence angles in the upper hemisphere:

$$I_{ri}(\theta_l, \phi_l) = \int_0^{\pi/2} \sin \theta_i d\theta_i \int_0^{2\pi} d\phi_i \frac{\cos \theta_i}{4\pi \cos \theta_l} \left[ \begin{array}{l} \gamma_{vvvv}^i(\theta_l, \phi_l; \theta_i, \phi_i) + \gamma_{vhvh}^i(\theta_l, \phi_l; \theta_i, \phi_i) \\ \gamma_{hhhh}^i(\theta_l, \phi_l; \theta_i, \phi_i) + \gamma_{hv hv}^i(\theta_l, \phi_l; \theta_i, \phi_i) \\ 2\text{Re}(\gamma_{vh hh}^i(\theta_l, \phi_l; \theta_i, \phi_i) + \gamma_{vv hv}^i(\theta_l, \phi_l; \theta_i, \phi_i)) \\ 2\text{Im}(\gamma_{vh hh}^i(\theta_l, \phi_l; \theta_i, \phi_i) + \gamma_{vv hv}^i(\theta_l, \phi_l; \theta_i, \phi_i)) \end{array} \right] \quad (16)$$

The bistatic scattering coefficients are related to the wavenumber spectrum  $W$  of sea surfaces by

$$\gamma_{\alpha\beta\mu\nu}^i(\theta_l, \phi_l; \theta_i, \phi_i) = \frac{F_{\alpha\beta\mu\nu}(\theta_l, \phi_l; \theta_i, \phi_i)}{\cos \theta_i} \frac{W(k_\rho \cos \phi_l - k_{\rho i} \cos \phi_i, k_\rho \sin \phi_l - k_{\rho i} \sin \phi_i)}{\cos \theta_i} \quad (17)$$

with  $\alpha, \beta, \mu$ , and  $\nu$  being either  $v$  or  $h$ .

Here,  $\theta_l$  and  $\phi_l$  signify the zenith and azimuth angles of the propagation direction of scattered waves in the local surface coordinate, and  $\theta_i$  and  $\phi_i$  the zenith and azimuth angles of the propagation direction of the incident wave. The wavenumbers,  $k_\rho = k_0 \sin \theta_l$  and  $k_{\rho i} = k_0 \sin \theta_i$ , are the magnitudes of the scattered and incident wave vectors projected on the horizontal plane.  $k_0$  is the free-space electromagnetic wavenumber. The expressions of scattering coefficients,  $R_{\alpha\beta\mu\nu}$ , are given in Appendix B.

The coherent reflectivity  $I_{rc}$  with corrections by the second order scattered fields is expressed as [4]

$$I_{rc} = \begin{bmatrix} |R_{vv}^{(0)}|^2 + 2\text{Re}(R_{vv}^{(0)} R_{vv}^{(2)*}) \\ |R_{hh}^{(0)}|^2 + 2\text{Re}(R_{hh}^{(0)} R_{hh}^{(2)*}) \\ 2\text{Re}(R_{vh}^{(2)} R_{hh}^{(0)*} + R_{vv}^{(0)} R_{hv}^{(2)*}) \\ 2\text{Im}(R_{vh}^{(2)} R_{hh}^{(0)*} + R_{vv}^{(0)} R_{hv}^{(2)*}) \end{bmatrix} \quad (18)$$

Here,  $R_{vv}^{(0)}$  and  $R_{hh}^{(0)}$  are the Fresnel reflection coefficients for vertically and horizontally polarized incident fields, respectively, and  $R_{\alpha\beta}^{(2)}$  with  $\alpha$  and  $\beta$  being  $v$  or  $h$  is the correction of specular reflection coefficients caused by the small surface perturbation [4]:

$$R_{\alpha\beta}^{(2)}(\theta_i, \phi_i) = \int_0^{2\pi} \int_0^\infty k_0^2 W(k_{\rho i} \cos \phi_i - k_\rho \cos \phi, k_{\rho i} \sin \phi_i - k_\rho \sin \phi) g_{\alpha\beta}^{(2)} k_\rho dk_\rho d\phi \quad (19)$$

where  $k_{\rho i} = k_0 \sin \theta_i$  is the transverse component of the incident wavenumber, and the expression of  $g_{\alpha\beta}^{(2)}$  is given in Appendix C. It should be noticed that the above equation provides the correction coefficients for arbitrary incidence and azimuth angles ( $\theta_i$  and  $\phi_i$ ). To use it consistently with the Kirchhoff's law, substitute  $\theta_i$  and  $\phi_i$  by the observation angles  $\theta_l$  and  $\phi_l + \pi$  in Eq. (15). This is because only the waves incident from the direction  $(\theta_i, \phi_i + \pi)$  can be specularly reflected into the observation direction  $(\theta_l, \phi_l)$ .

### 3.3 Emission from foam

Although foam typically covers only a few percents of sea surfaces, increasing foam coverage on the sea surface can substantially increase the sea surface emissivity [26, 27]. Previous theoretical foam scattering models, although having offered physical insight into the excess

brightness temperature contribution by sea foam, are not yet accurate enough to predict the polarization properties and incidence angle dependence of microwave emission from foam. Further research on the polarization signatures of foam is imperative.

Due to the lack of a quantitative theoretical scattering model for foam, Stogryn's empirical emissivity model of sea foam [26] is used to calculate the emissivities of vertical and horizontal polarizations in the local surface coordinate. The Stokes vector in the local surface coordinate is then transformed to  $I_{sf}$  in the earth surface coordinate using the coordinate transformation described in Appendix A.

## 4 Comparison with experimental data

In this section, the wind direction signals in microwave brightness temperatures of sea surfaces are interpreted using the two-scale model described in the previous section. The theoretical results from the two-scale model are compared with the data from [11, 12, 15, 14].

Model inputs required for theoretical calculations include the surface spectrum  $W$  and the sea surface permittivity. The wind-induced surfaces are described by an empirical surface spectrum  $W$  proposed by Durden and Vesecky [28]. (Because some typographical errors are found in their paper, the correct expressions of these formulas are shown in Appendix I.) The choice of this spectrum, instead of many other forms of sea spectrum, for investigating sea surface brightness temperatures is because theoretical backscattering coefficients calculated using this spectrum function were shown to agree reasonably well with many aircraft scatterometer measurements [28] and the total slope variances of the surface agree with Cox and Munk's measurements. However, results from several studies [3, 10, 33, 34] suggest that Cox and Munk's slope variances might be an underestimate for sea surfaces, 'Table 1 summarized the slope variances of sea surfaces at a wind speed of 9 m/s at 5 m elevation from these studies. To make the slope variances closer to these studies, the magnitude ( $a_0$ ) of Durden and Vesecky's surface spectrum has to be raised from 0.004 to 0.008. It is found that this adjustment is also necessary to make the theoretical results from the two-scale model

more comparable with the data. Hence,  $a$ , of 0.008 is used for the model calculations in this paper. Another input to the theoretical model is the permittivity of sea water, which is calculated using Klein and Swift's dielectric model of sea surfaces [29] with the measured water temperature by NOAA buoys and an assumed salinity of 35 parts per thousand.

A key parameter in the two-scale model is the wavenumber cutoff  $k_d$ . This cutoff wavenumber is selected in such a way that the rms height of short-scale waves is valid for the small perturbation method and the curvature of large-scale waves allows the use of the GO model. Table 2 illustrates the rms slopes ( $S_u$  and  $S_c$ ) of large scale waves and rms height ( $\sigma$ ) of small-scale waves for two cutoff wavenumbers used for the sensitivity analysis of the theoretical results on  $k_d$ . The harmonic coefficients of all Stokes parameters [Eqs. (2) to (5)] are calculated from  $0^\circ$  to  $70^\circ$  incidence using both cutoff wavenumbers. The rms difference averaged over incidence angles and the worst case difference among all incidence angles are presented in Table 3. The sensitivities of  $T_{v0}$  and  $T_{h0}$  to  $k_d$  are much smaller than the magnitudes of  $T_{v0}$  and  $T_{h0}$ . The rms difference is typically about 0.1 K or smaller for the first and second harmonic coefficients. The results show that the theoretical results from the two-scale model are insensitive to the cutoff wavenumber  $k_d$ . Therefore, only theoretical results with  $k_d$  equal to  $120 \text{ rad/m}$  for 19.35 GHz and  $230 \text{ rad/m}$  for 37 GHz are illustrated in the following analysis.

Figure 2 illustrates theoretical  $T_{v0}$  and  $T_{h0}$  versus incidence angles for several wind speeds. The zeroth harmonic coefficients calculated from the SSM/I geophysical model function by Wentz [12] are also included for comparison. There is a good agreement between the theory and the SSM/I geophysical model function by Wentz [12]. As shown, the wind speed sensitivities of  $T_{v0}$  are positive at low incidence angles and negative at incidence angles larger than  $60^\circ$ , consistent with the experimental data reported in [1, 2] and the theoretical results [9]. Theoretical 19 GHz  $T_{v0}$  reaches almost no wind speed sensitivity at  $55^\circ$ , while 37 GHz  $T_{v0}$  at a smaller incidence angle of about  $50^\circ$ . This is because the dielectric constant of sea surfaces are smaller at 37 GHz, resulting in a smaller Brewster angle and consequently,

a smaller incidence angle where the wind speed sensitivity of  $T'_{v0}$  makes a transition from positive to negative numbers. Note that although the wind speed sensitivity of  $T'_{v0}$  in Wentz's SSM/I geophysical model is small, it remains positive at 37 GHz, inconsistent with the small negative sensitivity from the model predictions. However, Hollinger's 19 GHz data [1] showed that there is no wind speed sensitivity at about 60° incidence angles, while the  $T_v$  data from Sasaki et al. [2] showed a zero crossing at about 55°. This suggests that the small wind speed sensitivity of  $T'_{v0}$  between 50° and 60° could be sensitive to other surface parameters, like the sea surface dielectric constant as well as the area] coverage and brightness properties of sea foam. Further refinements of these model inputs could be necessary to achieve a better accuracy for  $T'_{v0}$  between 50° and 60° incidence angles. Unlike the vertical polarization,  $T'_{h0}$  is a monotonic increasing function of wind speeds at all incidence angles. Theoretically  $T'_{h0}$  has a slightly larger wind speed sensitivity at higher incidence angles. This suggests that a spaceborne radiometer operating at a larger incidence angle could provide a better accuracy for wind speed measurements than at lower incidence angles. However, it should be aware that the atmospheric radiation and attenuation, which become more significant at large incidence angles, will place an upper limit on the useful range of incidence angles for spaceborne observations.

Figures 3 to 5 compare the azimuthal variations of theoretical and measured Stokes parameters over a 360° circle. The up and downwind directions are represented by 0° and 180°. To highlight the wind direction dependence, all zeroth harmonic terms ( $T'_{v0}$  and  $T'_{h0}$ ) have been subtracted from theoretical and experimental data and are illustrated in Table 4. The difference between the theoretical and experimental  $T'_{v0}$  indicates the contribution of atmospheric radiation and attenuation. At 45° incidence, the difference is about 201K corresponding to an atmospheric attenuation of about 0.3 dB, which is consistent with the fact that the experimental data illustrated were measured under clear sky conditions. This suggests that the atmospheric attenuation has a negligible effect on the wind direction signals in these cases. However, the influence of atmospheric radiation on  $T'_{h0}$  increases with

increasing angles. This is partly due to the longer path length through the atmosphere and partly due to the larger surface reflectivity at higher incidence angles tending to reflect more horizontally polarized sky radiation. The illustrated atmospheric attenuation and radiation estimated from the above comparison are consistent with those estimated from [35] for the standard US atmosphere.

Figure 3 illustrates the comparison of theory and data at 30° incidence angle. The data were measured using an aircraft K-band (19.35 GHz) polarimetric radiometer [15]. As observed in theoretical and experimental data,  $T_v$  and  $T_h$  have an even symmetry with respect to the wind direction, while  $U$  has an odd symmetry. These signatures agree with the symmetry properties derived from Maxwell's equations for media with reflection symmetry [23]. There are two peaks located at the up (0°) and downwind (180°) directions and two minima approximately at the crosswind directions (90° and 270°) in  $T_v$  data. This is similar to that in backscatter data measured with microwave scatterometers. However,  $T_h$  data, with a phase signature opposite to that in  $T_v$  data have local minima at up and downwind directions. The angular dependence in these three Stokes parameters agrees very well with that from the two-scale model.

Figure 4 illustrates theoretical data along with dual-frequency (19 and 37 GHz) measurements made at 55° incidence angle [15]. Also included in this figure are  $T_v$  and  $T_h$  data calculated from Wentz's SSM/I geophysical model function [12]. There is a good agreement between theoretical and experimental data for all Stokes parameters in terms of the magnitudes of azimuthal modulations and their symmetry properties with respect to the wind direction. What is interesting in this figure is that the wind direction signals in measurements as well as theoretical results are insensitive to frequencies from 19 to 37 GHz. This can be attributed to the multiple scale nature of wind waves. If scaled by the electromagnetic wavelength, the wind waves dominating the electromagnetic scattering at 19 and 37 GHz would appear similar at these two frequencies. Under the assumptions that the capillary wavenumber spectrum behaves like  $1/k^4$  and that the angular variation of wavenumber



spectrum remains constant, the weak frequency dependence can be derived from the theory with a fixed  $k_d/k_0$  for theoretical calculations. This is because after a change of integration variable from the absolute wavenumber  $k_p$  to a normalized wavenumber  $k_p/k_0$ , the coherent and incoherent reflectivities [Eqs. (17) and (18)] were shown to have a weak frequency sensitivity [15]. “In this theoretical model, the weak frequency dependence is caused by the deviation of wavenumber spectrum from  $1/k^4$  and the sensitivity of sea surface permittivity to frequency.

Another interesting point is that  $T_v$  and  $U$  from both theory and data illustrated in Fig. 4 oscillate only once over a  $360^\circ$  change of wind direction, while  $T_h$  and  $V$  oscillate twice over  $360^\circ$ . These signatures are very different from those shown in Fig. 3. The peak at the downwind direction observed in  $T_v$  at  $30^\circ$  incidence angle does not appear in either data or theory at  $55^\circ$  incidence angle, and the peak (dip) of  $U$  at about  $135^\circ$  ( $225^\circ$ ) almost disappear. These changes can be explained by the Bragg scattering and the hydrodynamic modulation mechanisms. As discussed in Section 5, the Bragg scattering mechanism predicts a small  $\cos 2\phi$  signal in  $T_v$  at near  $55^\circ$  incidence angles, but the hydrodynamic modulation characterized by Eq. (11) introduces a positive up and downwind brightness difference (see Section 5.1). Hence, the directional  $T_v$  signal has a dominant  $\cos \phi$  signature, instead of a  $\cos 2\phi$  modulation like that seen in  $T_h$ . Similar reduction of the second-harmonic signal in  $U$  with increasing incidence angles is also a result of the hydrodynamic modulation mechanism. These observations imply a very useful application of the polarimetric signals for the measurement of surface directional spectra. As shown,  $T_v$  is more sensitive to the up/downwind asymmetric surface features and less sensitive to the up/crosswind asymmetry, while the opposite is true for  $T_h$ . These two characteristics are complementary and directly indicate the relative magnitudes of orthogonal harmonic components in the directional wave spectrum.

Figure 5 compares data and theory at the incidence angle of  $65^\circ$  for all Stokes parameters. Weak frequency sensitivity is observed just like the data collected at smaller incidence angles and can be explained by the self-similar characteristics of surfaces using the theoretical model.

The major difference between this set of data and those at lower incidence angles is that  $T_v$  dips at the upwind direction, unlike that illustrated in Figs. 3 and 4. There is also a change of shape from low to high incidence angles in  $U$  data. These are consistent, with the signatures of Bragg scattering discussed in Section 5, where the  $T_v$  dip at the upwind direction is explained by a small negative  $\cos 2\phi$  signal from the Bragg scattering mechanism. Overall, the azimuthal signatures of all Stokes parameters are modeled very well by this two-scale model over a large range of incidence angles.

The above comparisons are for the JPL WINDRAD data from one of several continuous 360° circles. To make a more quantitative comparison, the data from two sets of continuous circles have been used to compute the harmonic coefficients of wind direction signals. Each set of continuous circles consists of three circles each for 45° and 55° incidence and two circles for 65° incidence. Figures 6 and 7 plot the first and second harmonic coefficients of all Stokes parameters as a function of incidence angles at 19 and 37 GHz, respectively. Also included are the 14 GHz and 37 GHz measurements by Etkin et al. [1] and Dzura et al. [13] at near normal incidence ( $\leq 10^\circ$ ) and Wentz's  $T_v$  and  $T_h$  model coefficients for the SSM/I at 53° incidence angle [12]. It can be seen that the harmonic coefficients calculated from the two-scale model agree well with the experimental data over a large range of incidence angles. This suggests that dominant scattering mechanisms contributing to the directional signatures of sea surface brightness temperatures have been considered in the two-scale scattering model.

Results from the geometric optics model using Cox and Munk's slope distribution are included in Figures 6 and 7 for comparison. The geometric optics model are obtained by using Cox and Munk's slope distribution for the probability function  $P$  in Eq. (7) and by calculating  $I_{sl}$  from tilted flat water surfaces. It is seen that the GO model with Cox and Munk's distribution significantly underestimates all harmonic coefficients from small to middle range of incidence angles and overestimates  $U_2$  at above 65° incidence angles.

A crucial drawback of the GO model is its prediction of the fourth Stokes parameter  $V$ , which have never been measured for sea surfaces before until 1994 by JPL [15]. Although  $V$

is smaller than the other Stokes parameters, there are clear wind direction signals illustrated in Figures 4 and 5, in particular at large incidence angles. However, the theoretical results from the GO model are zero for all observation angles. This is because the fourth Stokes parameter  $V$  is zero for the emission from a flat surface. Since  $V$  is invariant under any coordinate rotation,  $V$  remains zero for any tilted flat surface. As a result, calculating the brightness temperatures as a weighted sum of microwave emissions from randomly tilted flat surfaces, the GO model fails to predict the measured value of  $V$  from the JPL experiment. The failure of the GO model is due to the neglect of Bragg scattering effects by short waves, which was taken into account by the two-scale model.

## **5 Effects of Scattering Mechanisms**

Given the reasonable agreement between the two-scale model and the experimental data illustrated in the previous section, the relative contributions of hydrodynamic modulation, small and large scale waves on the directional signatures of brightness temperatures are investigated using the theoretical two-scale model. Several features regarding the variation of wind directional signals over the incidence angle will be discussed.

### **5.1 Hydrodynamic modulation**

The general signature of the theoretical prediction is that the first harmonic coefficients are zero at normal incidence [4] and increase with increasing incidence angles. This is because the geometries for up and downwind observation directions degenerate into one at the normal incidence angle, resulting in no up/downwind brightness asymmetry. As the incidence angle differs from zero, the asymmetric surface features in the leeward and windward sides of the large-scale waves provide uneven contributions to the brightness temperatures at the up and downwind observation directions. Evidently, increasing difference between the up and downwind observation geometries leads to larger first harmonic coefficients at higher incidence angles.

in the two-scale model described here, the first harmonic coefficients are caused by the hydrodynamic modulation of the capillary waves by large scale waves, with capillary waves rougher in the leeward side of the large waves than those in the windward face. The effects of this phenomenon can be more easily understood by a simple model discussed below. In particular, we will discuss why  $T_v$  has a positive up/downwind asymmetry at all incidence angles and that of  $T_h$  becomes positive at high incidence angles.

Consider the simple model illustrated in Figure 8 where there are two surface facets, denoted by  $A$  and  $B$  with slopes equal to  $\pm S$ . These two facets represent the windward and leeward faces of large-scale waves. For simplicity, it is assumed that there are capillary waves riding on facet  $B$ , but not on facet  $A$ . From Eq. (7),  $T_v$  for this simple model at the upwind and downwind observation directions can be written as

$$T_{v,up} = \frac{1}{2}[T_{1v}(1 + S \tan \theta) + T_{2v}(1 - S \tan \theta)] \quad (20)$$

$$T_{v,down} = \frac{1}{2}[T_{3v}(1 - S \tan \theta) + T_{4v}(1 + S \tan \theta)] \quad (21)$$

Hence, the up/downwind brightness asymmetry is

$$T_{v,up} - T_{v,down} = \frac{1}{2}(T_{1v} - T_{4v})(1 + S \tan \theta) - \frac{1}{2}(T_{3v} - T_{2v})(1 - S \tan \theta) \quad (22)$$

If  $\theta = \tan^{-1} S$ ,  $T_{1v} - T_{4v}$  represents the change of brightness temperatures due to the small-scale roughness on facet  $B$  at a local incidence angle of  $\theta - \psi$ , and  $T_{3v} - T_{2v}$  the change of the brightness temperatures at a local incidence angle of  $\theta + \psi$ .

From Fig. 2, the wind speed sensitivity of  $T_{v0}$  decreases with increasing incidence angles. This implies that  $T_{1v} - T_{4v} > T_{3v} - T_{2v}$ . Thus,  $T_v$  has a positive up/downwind asymmetry. In particular, for the special case that the incidence angle is near the angle where  $T_{v0}$  is insensitive to the wind speed (550). The wind speed sensitivity of  $T_{v0}$  illustrated in Fig. 2 indicates

$$T_{1v} > T_{4v} \quad (23)$$

$$T_{2v} > T_{3v} \quad (24)$$

for  $\theta$  near  $55^\circ$ . Hence, there is a positive up/downwind asymmetry in  $T'_v$ .

Unlike  $T'_{v0}$ , the wind speed sensitivity of  $T'_{h0}$  is positive and remains almost like a constant over a large range of incidence angles. This suggests that

$$T'_{1h} - T'_{4h} \approx T'_{3h} - T'_{2h} > 0 \quad (25)$$

Hence,

$$T'_{h,up} - T'_{h,down} \approx (T'_{1h}T'_{4h})S \tan \theta + [(T'_{1h} - T'_{4h}) - (T'_{3h} - T'_{2h})] \quad (26)$$

The first term on the right hand side of the equation is positive and increases with increasing incidence angles, while the second term in the brackets is a small negative quantity because  $T'_{h0}$  has a slightly larger wind speed sensitivity at higher incidence angles according to Figure 2. This indicates that the up/downwind asymmetry of  $T'_h$  is small and negative at small incidence angles and becomes positive at large incidence angles when the positive asymmetry proportional to  $S \tan \theta$  overcomes the negative asymmetry contributed by the second term.

From this simple model, it is shown that the up/downwind asymmetries of  $T'_v$  is always positive and that of  $T'_h$  increases with increasing incidence angles. Additionally, because the slope of large-scale sea surfaces is small, it is likely that the up/downwind asymmetry of  $T'_h$  is smaller than that of  $T'_v$ . This is consistent with the experimental observations illustrated in Figures 6 and 7.

However, Figures 6 and 7 indicates that the asymmetry of  $T'_v$  is underestimated by the two-scale model. Several factors might cause the discrepancy observed between data and theory. One is the limited numerical accuracy of the two-scale model, which is after all an approximate numerical model for calculating the scattering from multi-scale surfaces and may not be accurate enough in considering the scattering from waves near the two-scale cutoff and the interaction between small and large-scale waves. Secondly, the empirical formula for hydrodynamic modulation described by Eq. (11) is expected to be too simplistic, and better characterization of the modulation process on the magnitudes of short waves distributed on the long waves is necessary. Finally, although the two-scale model described

here has included Stogryn's sea foam model in the calculation of brightness temperatures, the anisotropic brightness of the whitecaps [27] has not been taken into account. Data from [27] measured at the nominal incidence angle of  $50^\circ$  indicated radiometrically brighter sea foam in the leeward side of the large waves than that in the windward face [27], with the 37-GHz  $T_h$  exhibiting twice the sensitivity to sea foam than the 37 GHz  $T_v$ . This indicates that the polarized microwave emission from sea foam has a stronger influence on  $T_h$  than  $0.11 T_v$ . But note that this information does not tell us the influence of sea foam on the the up/downwind brightness asymmetry. To understand the contribution of sea foam to the up/downwind asymmetry, it is necessary to know two terms, including the difference of up and downwind brightness temperatures of sea foam in the leeward face and that in the windward face. It is the sum of these two terms representing the up/downwind asymmetry. The present sea foam emission models and the data from [27] do not allow us to explore the contributions by sea foam to the up and downwind asymmetry. Further experimental study of the polarimetric radiometric signatures of sea foam at all azimuth angles is necessary.

## 5.2 Geometric Optics versus Bragg scattering

To examine the relative contributions of large waves, small waves and foam in the two-scale model, the Stokes parameters are calculated for three cases: (i) small-scale waves with the spectrum  $W_s$  specified by Eq. (10), (ii) large waves characterized by the surface spectrum  $W_l$ , and (iii) large waves with foam. Specifically, the Stokes vector for case (i) is calculated using Eq. (14), and that for case (iii) is calculated using Eq. (7) with  $I_{ss}$  replaced by that of a tilted flat surface. The fractional coverage of sea foam is calculated using the formula discussed previously. Case (ii) is a special case of case (iii) with  $F_r = 0$ . The second harmonic coefficients for these three cases are illustrated in Figure 9. (Note that there is no up and downwind asymmetry in the small and large scale waves, and thus, theoretical first harmonic coefficients are zero. ) As shown, the contributions of large waves and sea foam are small and the curves for case (iii) are almost identical to those for case (ii), indicating that the sea

foam model considered in this paper has negligible contribution. Additionally, the directional signals in all Stokes parameters predicted by the two-scale model are shown to be dominated by small waves. In particular, as discussed previously, theoretical  $V_2$  from the GO model is zero, while the contribution by the Bragg scattering mechanism is very close to that from the two-scale model. The above comparison suggests that Bragg scattering mechanism is the primary scattering source for the directional signals in sea surface brightness temperatures.

### 5.3 Signatures of Bragg Scattering

A very interesting signature of the Bragg scattering mechanism illustrated in Figure 9 is that  $T_{v2}$  and  $U_2$  change sign between  $50^\circ$  and  $70^\circ$  incidence angles, but no similar phase change is found in  $T_{h2}$  and  $V_2$ . The sign change of  $T_{v2}$  means that  $T_v$  has a positive up/crosswind asymmetry at small incidence angles, but negative at large incidence angles. This kind of phase change cannot be found in the microwave backscatter from sea surfaces. However, this signature is similar to the wind speed sensitivities of  $T_{v0}$  and  $T_{h0}$  observed in the experimental data [1, 2] and the theoretical results plotted in Figure 2. The wind speed sensitivity of  $T_{v0}$  is positive at small incidence angle, and is negative at larger than  $60^\circ$  incidence angles. This has been explained by the effects of Brewster angle of sea surfaces. At this angle, which is near  $80^\circ$  for sea surfaces,  $T_v$  of a flat water surface reaches the maximum as a function of incidence angles. Roughening the surface by wind forcing increases the surface reflectivity or reduces the surface emissivity for vertical polarization at the Brewster angle. Thus, the wind speed sensitivity of  $T_{v0}$  changes sign at about  $55^\circ$  to make a continuous transition from positive at low incidence angles to negative at high incidence angles. This suggests that  $T_v$  is not sensitive to the Bragg waves at near  $55^\circ$  incidence angle, and consequently implies that the Bragg wave will produce small directional  $T_v$  signal near this angle.

To verify that the sign change is not a numerical artifact of the small perturbation method (SPM), Monte Carlo simulations of scattering from one dimensional periodic rough surfaces with a power-law spectrum is carried out for incidence angles between  $40^\circ$  and  $70^\circ$ . In

simulating the periodic rough surfaces, the surface spectra] density function is assumed to have a discrete  $1/k^3$  spectrum.

$$W(k_x, k_y) = g \sum_{n=1}^{10} k_x^{-3} \delta(k_x - nk_l) \delta(k_y) \quad (27)$$

where  $\delta$  is the delta-function, and  $k_l = 2\pi/5\lambda$  is the low-wavenumber cutoff. Here  $\lambda$  is the electromagnetic wavelength. Independent random numbers with the Gaussian distribution are generated for the real and imaginary parts of each Fourier component of the surfaces and further weighted by the desired spectral density  $k_x^{-3/2}$ . The simulated Fourier spectra are then transformed to the spatial domain by the FFT. Each simulated surface is  $5\lambda$  long and has 40 samples per wavelength. Ten surfaces are generated, and the factor 'g' is adjusted for the desired rms surface height ( $u$ ). The surfaces simulated by this approach are periodic with a period corresponding to the low-wavenumber cutoff. To solve the scattering coefficients of all the reflected Floquet modes for both horizontally and vertically polarized incident waves, the Method of Moment with triangular basis functions for surface tangential fields and pulse weighting is used. Once the scattering coefficients are obtained, the Stokes vectors of the thermal emission from the simulated random surfaces are calculated using the Kirchhoff's law. Finally, the average is taken over these ten realizations to represent the Stokes vector of the random rough surfaces. Extensive comparison of the numerical Monte Carlo simulations and the small perturbation method can be found in [4].

Figures 10 and 11 illustrate the comparison between the results of this Monte Carlo simulation and the SPM at  $40^\circ$  and  $70^\circ$  incidence angles. The results of SPM agree very well with the numerical technique. (The spikes observed in the figures at several azimuth angles are the typical scattering features of periodic surfaces [4], and are not anticipated from natural ocean surfaces. ) The significance of the numerical simulations is that the azimuthal signatures of all Stokes parameters are similar to those observed in the experimental data.  $T_v$  at  $\phi = 0^\circ$  (upwind direction) is larger than that at  $\phi = 90^\circ$  (crosswind direction) at  $40^\circ$  incidence angle, while the opposite is observed at  $70^\circ$  incidence angle. Additionally,  $U$  at  $45^\circ$  azimuth angle is negative at  $40^\circ$  incidence angle and positive at  $70^\circ$ . These correspond to the



sign changes of  $T_{v2}$  and  $U_2$  from low to high incidence angles discussed previously. In summary, the numerical simulations lend support to the accuracy of the SPM and indicate that the second harmonics (up and crosswind asymmetry) of wind direction signals obtained from the two-scale model for all polarization channels are primarily due to the Bragg scattering in the frequency range of 19 to 37 GHz.

## 6 Summary

The wind direction signals in the brightness temperatures of sea surfaces are analyzed and examined using a two-scale scattering model. This model accounts for the tilting effects of large-scale waves, the anisotropic wavenumber spectrum of short waves, hydrodynamic modulations characterizing the wind-wave interactions, and the excess microwave emission from sea foam. Model simulations are found to agree very well with the experimental data, from  $0^\circ$  to  $65^\circ$  incidence angles at 19 and 37 GHz. The weak frequency dependence of the wind direction signals is explained by the multi-scale self-similar characteristics of the wind-roughened sea surfaces.

Relative contributions of the Bragg scattering by short waves and geometric tilting effects by long waves are examined. It is found that the GO model significantly underestimates the wind direction signals in all Stokes parameters. Furthermore the fourth Stokes parameter from the GO model is zero for all frequencies and incidence angles, in disagreement with the experimental data. In contrast, the Bragg scattering mechanism is the dominant contributing factor of the second harmonic coefficients of wind direction signals in the two-scale model. In particular, the phase reversal of  $T_{v2}$  and  $U_2$  between moderate and high incidence angles is shown to be a signature of the Bragg scattering mechanism. This signature is further corroborated by the numerical Monte Carlo simulations of scattering from one-dimensional periodic rough surfaces.

In the two-scale model, the up and downwind asymmetry of brightness temperatures is modeled by the hydrodynamic modulations of short waves by the long waves. Although the

trend of the first harmonic coefficients of the Stokes parameters as functions of incidence angles agrees with the experimental data, several improvements to the theoretical modeling of polarimetric sea surface brightness temperatures appear to be necessary. The most likely model components for improvement include the hydrodynamic modulation model of wind-wave interactions and the brightness temperature model of sea foam. It is apparent that the hydrodynamic model described Eq. (11) is too simplistic for sea surfaces. For example, the present model does not account for how the short waves are distributed on the leeward side of long waves as a function of wind speeds. The second component for improvement is the sea foam emission model. The empirical emission model by Stogryn [26] did not characterize the potential dependence of sea foam properties on the slope of long waves indicated by the data from [27]. However, there are not yet any reliable physical model or experimental data sets, allowing a quantitative determination of sea foam brightness temperatures as a function of surface slopes. Finally, the present model does not consider the scattering by breaking waves. Although the areal coverage of breaking waves, like that of sea foam, is usually small, the strong scattering properties of breaking waves have been known to be significant for the microwave backscattering at high incidence angles. Finally, the effects of multiple scattering on the microwave emission from sea surfaces need to be studied. Multiple scattering is known to be important for sea surface scattering at high incidence angles.

## ACKNOWLEDGMENT

The research described in this paper was carried out by the Jet Propulsion laboratory, California Institute of Technology, under a contract with the National Aeronautics and Space Administration.

## A Local coordinate system and vector transformations

Given the  $x$  and  $y$  slopes of a tilted fiat surface,  $S_x$  and  $S_y$ , the surface normal can be written as:

$$\hat{z}_l = \frac{-S_x \hat{x} - S_y \hat{y} + \hat{z}}{\sqrt{S_x^2 + S_y^2 + 1}} \quad (28)$$

However, the surface normal can also be expressed in terms of the zenith and azimuth angles,  $\theta_n$  and  $\phi_n$ , by

$$\hat{z}_l = \sin \theta_n \cos \phi_n \hat{x} + \sin \theta_n \sin \phi_n \hat{y} + \cos \theta_n \hat{z} \quad (29)$$

Equating the above equations allows us to determine  $\theta_n$  and  $\phi_n$ .

Besides the surface normal  $\hat{z}_l$  of the tilted surface, the local  $x$  and  $y$  unit vectors, denoted by  $\hat{x}_l$  and  $\hat{y}_l$ , need to be defined. Because this paper assumes that positive  $x$  is in the wind direction, the  $\hat{x}_l$  vector is chosen to be on the  $x-z$  plane so that the center direction of wind-induced capillary waves on the tilted surface can be conveniently represented by  $\hat{x}_l$ .

$$\hat{x}_l = \cos \beta \hat{x} - \sin \beta \hat{z} \quad (30)$$

$$\hat{y}_l = \hat{z}_l \times \hat{x}_l \quad (31)$$

The angle  $\beta$  is determined by enforcing  $\hat{x}_l$  to be perpendicular to  $\hat{z}_l$ , resulting in

$$\beta = \arctan(\tan \theta_n \cos \phi_n) \quad (32)$$

Carrying out the cross product and using the solution of  $\beta$  give the explicit expression of  $\hat{y}_l$

$$\hat{y}_l = -\sin \theta_n \sin \phi_n (\sin \beta \hat{x} + \cos \beta \hat{z}) + \hat{y} \sqrt{1 - \sin^2 \theta_n \sin^2 \phi_n} \quad (33)$$

Note that as  $\theta_n$  continuous]  $y$  approaches zero, the  $x_l y_l z_l$  coordinate system approaches the global  $xyz$  coordinate system. Additionally, since  $\theta_n$  is expected to be small for sea surfaces,  $\hat{x}_l$  and  $\hat{y}_l$  differ from  $\hat{x}$  and  $\hat{y}$ , respectively, by a small quantity of the order of  $\theta_n^2$ .

By using the above equations, a matrix  $A$  can be defined to recast these vector relations into a matrix form

$$\begin{bmatrix} \hat{x}_l \\ \hat{y}_l \\ \hat{z}_l \end{bmatrix} = A \begin{bmatrix} \hat{x} \\ \hat{y} \\ \hat{z} \end{bmatrix} \quad (34)$$

Here  $A$  is a three-by-three matrix.

Hence, the wave vector  $\bar{k}$  expressed in the local coordinate is

$$\bar{k}_l = A\bar{k} \quad (35)$$

From  $\bar{k}_l$ , the local incidence angle  $\theta_l$  and the local azimuth angle  $\phi_l$  can be calculated by the following relation

$$\bar{k}_l = \sin \theta_l \cos \phi_l \hat{x}_l + \sin \theta_l \sin \phi_l \hat{y}_l + \cos \theta_l \hat{z}_l \quad (36)$$

Additionally, the horizontal and vertical polarization vectors,  $\hat{h}_l$  and  $\hat{v}_l$ , can be defined in the local coordinate in terms of  $\bar{k}_l$  and  $\hat{z}_l$

$$\hat{h}_l = \frac{\bar{k}_l \times \hat{z}_l}{|\bar{k}_l \times \hat{z}_l|} \quad (37)$$

$$\hat{v}_l = \frac{\hat{h}_l \times \bar{k}_l}{|\hat{h}_l \times \bar{k}_l|} \quad (38)$$

Denoting the angle between  $\hat{h}$  and  $\hat{h}_l$  by  $\alpha$  results in

$$\cos \alpha = \hat{v} \cdot \hat{v}_l = \hat{h} \cdot \hat{h}_l \quad (39)$$

$$\sin \alpha = \hat{v} \cdot \hat{h}_l = -\hat{h} \cdot \hat{v}_l \quad (40)$$

The linearly polarized components of electric fields ( $E_v, E_h$ ) in the global coordinate are related to those ( $E_{vl}, E_{hl}$ ) in the local coordinate by

$$E_v = E_{vl} \cos \alpha + E_{hl} \sin \alpha \quad (41)$$

$$E_h = -E_{vl} \sin \alpha + E_{hl} \cos \alpha \quad (42)$$

Hence, it is straightforward to show that the Stokes parameters measured in the global coordinate are related to those measured in the local coordinate by

$$T_v = T_{vl} \cos^2 \alpha + T_{hl} \sin^2 \alpha - U_l \sin \alpha \cos \alpha \quad (43)$$

$$T_h = T_{vl} \sin^2 \alpha + T_{hl} \cos^2 \alpha - U_l \sin \alpha \cos \alpha \quad (44)$$

$$U = U_l(\cos^2 \alpha - \sin^2 \alpha) - (T_{vl} - T_{hl}) \sin 2\alpha \quad (45)$$

$$V = V_l \quad (46)$$

Subscript  $l$  indicates the quantities in the local coordinate.

## B First-order scattering coefficients

The coefficients for the incoherent bistatic scattering coefficients due to the first-order scattered fields are defined as:

$$F_{\alpha\beta\mu\nu}(\theta, \phi; \theta_i, \phi_i) = g_{\alpha\beta}^{(1)}(\theta, \phi; \theta_i, \phi_i) g_{\mu\nu}^{(1)*}(\theta, \phi; \theta_i, \phi_i) \quad (47)$$

with

$$g_{hh}^{(1)}(\theta, \phi; \theta_i, \phi_i) = \frac{2 \cos \theta_i (\epsilon - 1)}{(\cos \theta + \sqrt{\epsilon - \sin^2 \theta})(\cos \theta_i + \sqrt{\epsilon - \sin^2 \theta_i})} \cos(\phi - \phi_i) \quad (48)$$

$$g_{hv}^{(1)}(\theta, \phi; \theta_i, \phi_i) = \frac{2 \cos \theta_i (\epsilon - 1) \sqrt{\epsilon - \sin^2 \theta_i}}{(\cos \theta + \sqrt{\epsilon - \sin^2 \theta})(\epsilon \cos \theta_i + \sqrt{\epsilon - \sin^2 \theta_i})} \sin(\phi - \phi_i) \quad (49)$$

$$g_{vh}^{(1)}(\theta, \phi; \theta_i, \phi_i) = \frac{2 \cos \theta_i (\epsilon - 1) \sqrt{\epsilon - \sin^2 \theta}}{(\epsilon \cos \theta + \sqrt{\epsilon - \sin^2 \theta})(\cos \theta_i + \sqrt{\epsilon - \sin^2 \theta_i})} \sin(\phi - \phi_i) \quad (50)$$

$$g_{vv}^{(1)}(\theta, \phi; \theta_i, \phi_i) = \frac{2 \cos \theta_i (\epsilon - 1) \epsilon \sin \theta \sin \theta_i - \sqrt{\epsilon - \sin^2 \theta} \sqrt{\epsilon - \sin^2 \theta_i} \cos(\phi - \phi_i)}{(\epsilon \cos \theta + \sqrt{\epsilon - \sin^2 \theta})(\epsilon \cos \theta_i + \sqrt{\epsilon - \sin^2 \theta_i})} \quad (51)$$

## C Second-order scattering coefficients

The correction terms of the coherent reflection coefficients due to second-order scattered fields are given as follows:

$$g_{hh}^{(2)} = \frac{2 \cos \theta_i (\epsilon - 1)}{(\cos \theta + \sqrt{\epsilon - \sin^2 \theta})(\cos \theta_i + \sqrt{\epsilon - \sin^2 \theta_i})^2} \left\{ \sqrt{\epsilon - \sin^2 \theta_i} \right. \\ \left. - \frac{(\epsilon - 1)}{(\xi^2 + \sqrt{\epsilon - \xi^2} \sqrt{1 - \xi^2})(\sqrt{\epsilon - \xi^2} + \sqrt{1 - \xi^2})} \right. \\ \left. \left[ \sqrt{\epsilon - \xi^2} \sqrt{1 - \xi^2} (2 + \xi^2 \cos^2(\phi - \phi_i)) \right] \right\} \quad (52)$$

$$g_{hv}^{(2)} = \frac{2 \cos \theta_i (\epsilon - 1) \sin(\phi - \phi_i)}{(\cos \theta_i + \sqrt{\epsilon - \sin^2 \theta_i})(\epsilon \cos \theta_i + \sqrt{\epsilon - \sin^2 \theta_i})(\xi^2 + \sqrt{\epsilon - \xi^2} \sqrt{1 - \xi^2})} \left[ \epsilon \xi \sin \theta_i - \frac{(\epsilon - 1) \xi^2 \sqrt{\epsilon - \sin^2 \theta_i} \cos(\phi - \phi_i)}{(\sqrt{\epsilon - \xi^2} + \sqrt{1 - \xi^2})} \right] \quad (53)$$

$$g_{vh}^{(2)} = -g_{hv}^{(2)} \quad (54)$$

$$g_{vv}^{(2)} = \frac{2 \cos \theta_i (1 - \epsilon) \epsilon}{(\epsilon \cos \theta_i + \sqrt{\epsilon - \sin^2 \theta_i})^2} \left\{ \frac{(\epsilon - 1) \xi^2 \sin^2 \theta_i}{(\xi^2 + \sqrt{\epsilon - \xi^2} \sqrt{1 - \xi^2})(\sqrt{\epsilon - \xi^2} + \sqrt{1 - \xi^2})} + \sqrt{\epsilon - \sin^2 \theta_i} \left[ 1 - \frac{2 \xi \sin \theta_i \cos(\phi - \phi_i)}{\xi^2 + \sqrt{\epsilon - \xi^2} \sqrt{1 - \xi^2}} \right] - \frac{(\epsilon - \sin^2 \theta_i)(\epsilon - 1)}{\epsilon(\sqrt{\epsilon - \xi^2} + \sqrt{1 - \xi^2})} \left[ 1 - \frac{\xi^2 \cos^2(\phi - \phi_i)}{\xi^2 + \sqrt{\epsilon - \xi^2} \sqrt{1 - \xi^2}} \right] \right\} \quad (55)$$

where

$$\xi = \frac{k_\rho}{k_0} \quad (56)$$

## D Empirical sea surface spectrum

The surface spectrum for a fully developed ocean proposed by Durden and Vesecky [28] has the following form

$$W(k, \phi) = \frac{1}{2\pi k} S(k) \Phi(k, \phi) \quad (57)$$

where the portion of  $S(k)$  with  $k > k_j = 2$  was assumed by Durden and Vesecky based on the dimensional analysis:

$$S(k) = a_0 k^{-3} \frac{b k u_*^2}{(g_*)^{a \log_{10}(k/k_j)}} \quad (58)$$

with  $g_* = g + \gamma k^2$ ,  $\gamma = 7.25 \times 10^{-5}$ , and  $g = 9.81$ . Another three parameters for  $S(k)$  are  $a$ ,  $b$ , and  $a_0$ . The roll-off rate is controlled by  $a$  and  $b$ , and  $a_0$  represents the absolute magnitude of the spectrum. The values of  $a$ ,  $b$ , and  $a_0$  are chosen to be **0.225**, 1.25, and 0.008 to best fit the data.

For  $k < k_j = 2$ ,  $S(k)$  is described by the Pierson-Moskowitz spectrum

$$S(k) = b_0 k^{-3} \exp \left\{ -0.74 (k_c/k)^2 \right\} \quad (59)$$

with  $k_c = g/U_{19.5}^2$ .  $b_0$  is selected in such a way that  $S(k)$  is continuous at  $k = k_j$  for a given  $a_0$ .

The wind speed given at any elevation  $z$  can be calculated from the friction velocity  $u_*$  by

$$u(z) = \frac{u_*}{0.4} \log\left(\frac{z}{Z_0}\right) \quad (60)$$

where  $u_*$  is related to  $Z_0$  by

$$Z_0 = 0.0000684/u_* + 0.00428u_*^2 - 0.000443 \quad (61)$$

The angular portion of the spectrum is assumed to have the following form

$$\Phi(k, \phi) = 1 + C(1 - e^{-k'}) \cos 2\phi \quad (62)$$

The coefficients of the angular part of the spectrum are  $s = 1.5 \times 10^{-4}$  and

$$c = \frac{1 - R}{1 + R} \frac{2}{(1 - D)} \quad (63)$$

where

$$R = \frac{0.003 + 0.00192 U(12.5)}{0.00316 U(12.5)} \quad (64)$$

$$D = \frac{\int_0^\infty k^2 S(k) e^{-sk^2} dk}{\int_0^\infty k^2 S(k) dk} \quad (65)$$

There were misprints in the equations for  $Z_0$ ,  $c$ , and  $R$  in [28].

## References

- [1] Hollinger, J. P., "Passive microwave measurements of sea surface roughness," *IEEE Trans. Geosci. Electronics*, Vol. GE-9, No. 3, 165-169, July 1971.
- [2] Sasaki, Yasunori, Ichio Asanuma, Kei Muneyama, Gen'ichi Naito, and Tsutomu Suzuki, "The dependence of sea-surface microwave emission on wind speed, frequency, incidence angle, and polarization over the frequency range from 1 to 40 GHz," *IEEE Trans. Geosci. and Remote Sensing*, Vol. GE-25, No. 2, 138-146, March, 1987.
- [3] Donelan, M. A., and W. J. Pierson, "Radar scattering and equilibrium ranges in wind-generated waves with applications to scatterometry," *J. Geophys. Res.*, Vol. 92, No. c5, 4971-5029, May 15, 1987.
- [4] Yueh, S. H., R. Kwok, F. K. Li, S. V. Nghiem, W. J. Wilson, and J. A. Kong, "Polarimetric passive remote sensing of ocean wind vector," *Radio Science*, 799-814, July-August, 1994.
- [5] Stogryn, A., "The Apparent Temperature of the Sea at Microwave Frequencies," *IEEE Trans. Ant. Prop.*, Vol. AP-15, No. 2, 278-286, 1967.
- [6] Cox, C. S. and W. H. Munk, "Measurement of the roughness of the sea surface from photographs of the sun's glitter," *J. Opt. Soc. Am.*, Vol. 44, 838-850, 1954.
- [7] Semyonov, B.I., "Approximate computation of scattering of electromagnetic waves by rough surface contours," *Radio Eng. Electron Phys.*, 11, 1179-1187, 1966.
- [8] Wu, S. T., and A. K. Fung, "A noncoherent model for microwave emissions and backscattering from the sea surface," *J. Geophys. Res.*, Vol. 77, No. 30, 5917-5929, 1972.
- [9] Wentz, F. J., "A two-scale scattering model for foam-free sea microwave brightness temperatures," *J. Geophys. Res.*, Vol. 80, No. 24, 3441-3446, 1975.
- [10] Pierson, W. J., and R. A. Stacy, "The elevation, slope, and curvature spectra of a wind roughened sea surface," Contract Rep. NASA CR-2247, Langley Res. Center, NASA, Hampton, Va., Dec. 1973.
- [11] Etkin, V. S., M.D. Raev, M.G. Bulatov, Yu.A. Militsky, A.V. Smirnov, V.Yu. Raizer, Yu.A. Trokhimovsky, V.G. Irisov, A.V. Kuzmin, K.Ts. Litovchenko, E.A. Beshpalova, E.I. Skvortsov, M.N. Pospelov, and A.J. Smirnov, *Radiohydrophysical Aerospace Research of Ocean*, Report ИР-1749, Academy of Sciences, USSR, Space Research Institute, Moscow, 1991.
- [12] Wentz, Frank J., "Measurement of oceanic wind vector using satellite microwave radiometers," *IEEE Trans. Geosci. Remote Sensing*, Vol. 30, No. 5, 960-972, Sep., 1992.
- [13] Dzura, M. S., V. S. Etkin, A. S. Khrupin, M. N. Pospelov, and M. I. Raev, "Radiometers-Polarimeters: principles of design and applications for sea surface microwave emission polarimetry," *IEEE, Proceedings of International Geoscience and Remote Sensing Symposium*, Houston, 1992.
- [14] Yueh, S. H., W. J. Wilson, F. K. Li, W. R. Ricketts, and S. V. Nghiem, "Polarimetric measurements of sea surface brightness temperatures using an aircraft K-band radiometer," *IEEE Trans. Geosci. Remote Sensing*, Vol. 33, No. 1, 85-92, 1995.



- [15] Yueh, S. H., W. J. Wilson, F. K. Li, S. V. Nghiem, and W. B. Ricketts, "Polarimetric brightness temperatures of sea surfaces measured with aircraft K- and Ka-band radiometers," submitted for publication in *IEEE Trans. Geosci. Remote Sensing*, 1995.
- [16] Tsang, L., "Polarimetric passive remote sensing of random discrete scatterers and rough surfaces," *J. Electromagnetic Waves and Appl.*, Vol. 5, No. 1, 41-57, 1991.
- [17] Veyssoglu, M. E., S. H. Yueh, R. T. Shin, and J. A. Kong, "Polarimetric passive remote sensing of periodic surfaces," *J. Electromagnetic Waves and Appl.*, Vol. 5, No. 3, 267-280, 1991.
- [18] Yueh, S. H., R. Kwok, F. K. Li, S. V. Nghiem, W. J. Wilson, and J. A. Kong, "Polarimetric passive remote sensing of wind-generated sea surfaces and ocean wind vectors," *Proceedings of Ocean symposium*, Vol. 1, 31-36, Victoria, British Columbia, Canada, October 1993.
- [19] Nghiem, S. V., M. E. Veyssoglu, R. T. Shin, J. A. Kong, K. O'Neill, and A. Lohanick, "Polarimetric passive remote sensing of a periodic soil surface: microwave measurements and analysis" *J. Electromagnetic Waves and Appl.*, Vol. 5, No. 9, 997-1005, 1991.
- [20] Yueh, S. H., S. V. Nghiem, R. Kwok, W. J. Wilson, F. K. Li, J. T. Johnson, and J. A. Kong, "Polarimetric thermal emission from periodic water surfaces," *Radio Science*, Vol. 29, No. 1, 87-96, January -February, 1994.
- [21] Johnson, J. T., J. A. Kong, R. T. Shin, D. H. Staelin, K. O'Neill and A. W. Lohanick, "Third stokes parameter emission from a periodic water surface," *IEEE Trans. Geosci. Remote Sensing*, Vol. 31, No. 5, 1066-1080, September 1993.
- [22] Gasiewski, A. J., and Kunkee, "Polarized microwave emission from water- waves," *Radio Science*, Vol. 29, No. 6, 1449-1466, November-December, 1994.
- [23] Yueh, S. H., R. Kwok, and S. V. Nghiem, "Polarimetric scattering and emission properties of targets with reflection symmetry," *Radio Science*, Vol. 29, No. 6, 1409-1420, November-December, 1994.
- [24] Monahan, E., and I. G. O'Muircheartaigh, *Int. J. Remote Sensing*, Vol. 7, No. 5, 627-642, 1986.
- [25] Peake, W. H., "Interaction of electromagnetic waves with some natural surfaces," *IEEE Trans. Ant. and Prop.* Vol. AP-7, spec. suppl. 8324-8329, 1959.
- [26] Stogryn, A., "The Emissivity of Sea Foam at Microwave Frequencies," *J. of Geophys. Res.*, Vol. 77, No. 9, 1658-1666, 1972.
- [27] Smith, P. M., "The emissivity of sea foam at 19 and 37 GHz," *IEEE Trans. Geosci. and Remote Sensing*, Vol. GE-26, 541-547, 1988.
- [28] Durden, S. P., and J. F. Vesecky, "A physical radar cross-section model for a wind-driven sea with swell," *IEEE J. Oceanic Eng.*, Vol. OE-10, No. 4, 445-451, 1985.
- [29] Klein, L. A. and C. T. Swift, "An improved model for the dielectric constant of sea water at microwave frequencies," *IEEE Trans. Ant. and Prop.* Vol. AP-25, 104-111, 1977.

- [30] Hollinger, J. P., J. L. Peirce, and G. A. Poe, "SSM /1 Instrument Evaluation," *IEEE Trans. Geosci. Remote Sensing*, Vol. 28, No. 5, 781-790, Sept, 1990.
- [31] Yueh, S. H., S. V. Nghiem, and R. Kwok, "Comparison of a polarimetric scattering and emission model with ocean backscatter and brightness temperatures," *IEEE, Proceedings of International Geoscience and Remote Sensing symposium*, Pasadena, 1994. -
- [32] Yueh, S. H., and R. Kwok, "Electromagnetic fluctuations for anisotropic media and the generalized Kirchhoff's law," *Radio Science*, Volume 28, No. 4, pp. 471-480, July-August 1993.
- [33] Wentz, Frank, "Cox and Munk's Sea Surface Slope Variance," *J. of Geophy. Res.*, Vol. 81, No. 9, 1607-1608, 1976.
- [34] Ape], John R., "An improved model of the ocean surface-wave vector spectrum and its effects on radar backscatter," *J. of Geophy. Res.*, Vol. 99, No. c8, 16269-16291, August 1994.
- [35] Liebe, H. J., "An updated model for millimeter wave propagation in moist air," *Radio Science*, Vol. 20, No. 5, 1069-1089, 1985.

## List of Tables

- 1 Slope variances of sea surfaces normalized by Cox and Munk's for several sea surface spectra, The wind speed is 9 m/s at 5 m elevation, corresponding to 10.3 m/s at 19.5 m and 9.9 m/s at 12.5 m height based on Eq. (60 ). Cox and Munk's slope variance is the sum of  $S_u^2$  and  $S_c^2$ , which are calculated by  $S_u^2 = 0.00316 U(12.5)$  and  $S_c^2 = 0.003 + 0.00192 U(12.5)$ . . . . . 35
- 2 Slope variances of large scale waves are indicated by  $S_u^2$  and  $S_c^2$  at up and crosswind directions.  $\sigma$  is the rms height of small scale waves. The wind speed is 9 m/s at 5 m elevation, corresponding to 10.3 m/s at 19.5 m and 9.9 m/s at 12.5 m height based on Eq. (60 ). The magnitude of Durden and Vesecky's spectrum ( $a_0$ ) is .008. . . . . 35
- 3 Sensitivity of theoretical results on  $k_d$ : rms and the worst case difference between the harmonic coefficients calculated from two different  $k_d$  listed in Table 21 The wind speed is 9 m/s at 19.5 m elevation, and the sea surface temperature is 12° C..... . . . . 36
- 4 Theoretical and experimental  $T_{v0}$  and  $T_{h0}$ . Wentz's SSM /1 model [12] at 53° incidence were included for comparison. . . . . 36

	Normalized slope variance
Durden&Vesecky ( $a_0 = 0.004$ )	0.95
Durden&Vesecky ( $a_0 = 0.008$ )	1.9
Pierson&Stacy [9, 10]	> 2
Donelan&Pierson [3]	1.7
Apel [35]	2.5

Table 1: Slope variances of sea surfaces normalized by Cox and Munk's for several sea surface spectra. The wind speed is 9 m/s at 5 m elevation, corresponding to 10.3 m/s at 19.5 m and 9.9 m/s at 12.5 m height based on Eq. (60). Cox and Munk's slope variance is the sum of  $S_u^2$  and  $S_c^2$ , which are calculated by  $S_u^2 = 0.00316 U(12.5)$  and  $S_c^2 = 0.003 + 0.00192 U(12.5)$ .

Parameter	Durden&Vesecky				Cox&Munk
Frequency (GHz)	19.35		37		-
$k_0$ (1/m)	405.3		774.9		-
$k_d$ (1/m)	80	120	150	230	-
$S_u^2$	0.025	0.027	0.029	0.033	0.031
$S_c^2$	0.024	0.025	0.026	0.028	0.022
$k_0\sigma$	0.37	0.26	0.42	0.28	-

Table 2: Slope variances of large scale waves are indicated by  $S_u^2$  and  $S_c^2$  at up and crosswind directions.  $\sigma$  is the rms height of small scale waves. The wind speed is 9 m/s at 5 m elevation, corresponding to 10.3 m/s at 19.5 m and 9.9 m/s at 12.5 m height based on Eq. (60). The magnitude of Durden and Vesecky's spectrum ( $a_0$ ) is 0.008.

Frequency (GHz)	19.35		37	
Difference	RMS	WORST	RMS	WORST
$T_{v0}$	0.29	0.60	0.25	0.50
$T_{h0}$	0.32	0.60	0.37	0.70
$T_{v1}$	0.11	0.23	0.10	0.22
$T_{h1}$	0.07	0.14	0.10	0.18
$U_1$	0.07	0.18	0.11	0.28
$V_1$	0.00	0.01	0.00	0.01
$T_{v2}$	0.07	0.15	0.12	0.19
$T_{h2}$	0.04	0.13	0.11	0.30
$U_2$	0.08	0.15	0.13	0.25
$V_2$	0.04	0.12	0.05	0.15

Table 3: Sensitivity of theoretical results on  $k_d$ : rms and the worst case difference between the harmonic coefficients calculated from two different  $k_d$  listed in Table 2. The wind speed is 9 m/s at 19.5 m elevation, and the sea surface temperature is 12° C.

$\theta$	U@5m	Parameter	19.35 GHz			37GHz		
			Theory	Data	SSM/I	Theory	IEG	SSM/I
30	11 m/s	$T_{v0}$	<b>134.6</b>	160.7		<b>154.0</b>		
		$T_{h0}$	112.1	139.8		<b>130.0</b>		
45	9 m/s	$T_{v0}$	<b>150.7</b>	168.4		<b>170.4</b>	188.6	
		$T_{h0}$	96.5	121.2		<b>113.1</b>	144.0	
55	9 m/s	$T_{v0}$	168.4	186.4	167.6	187.3	204.7	187.2
		$T_{h0}$	<b>84.0</b>	116.6	85.6	99.3	141.0	<b>104.3</b>
65	9 m/s	$T_{v0}$	191.6	205.1		207.2	220.5	
		$T_{h0}$	69.5	116.2		83.0	142.5	

Table 4: Theoretical and experimental  $T_{v0}$  and  $T_{h0}$ . Wentz's SSM/I model [12] at 53° incidence were included for comparison.

## List of Figures

- 1 Configuration and coordinate system . . . . . 39
- 2  $T'_{v0}$  and  $T'_{h0}$  as functions of incidence angles for several wind speeds calculated from the two-scale model at 19.35 and 37 GHz frequencies.  $T'_{v0}$  and  $T'_{h0}$  from Wentz's SSM/I geophysical model function [12] are included for comparison. 39
- 3 Comparison of theoretical Stokes parameters with the aircraft K-band radiometer data at 30° incidence [14] as functions of azimuth angles. The buoy-measured surface temperature of  $T_s = 12$  degrees Celsius and the wind speed of 11 m/s at 5 m elevation are used in theoretical calculations. . . . . 40
- 4 Comparison of theoretical Stokes parameters with aircraft K- and Ka-band radiometer data at 55° incidence [15] as functions of azimuth angles. The buoy-measured surface temperature of  $T_s = 12$  degrees Celsius and the wind speed of 9 m/s at 5 m elevation are used in theoretical calculations. The SSM/I wind direction signals in  $T'_v$  and  $T'_h$  are also included for comparison. 41
- 5 Comparison of theoretical Stokes parameters with aircraft K- and Ka-band radiometer data at 65° incidence [15] as functions of azimuth angles. The buoy-measured surface temperature of  $T_s = 12$  degrees Celsius and the wind speed of 9 m/s at 5 m elevation are used in theoretical calculations. . . . . 42
- 6 Comparison of measured first and second harmonic coefficients with 2-scale and geometric optics models at 19.35 GHz. JPL's WINDRAD data were measured at a wind speed of 9 m/s at 5 m elevation, which is very close to the wind speed of 10 m/s at 19.5 m elevation for the measurements by Etkin et al. [11] and Dzura et al. [13].  $k_d = 150$  I/m and  $T_s = 12^\circ$  C. Cox and Munk's slope distribution is used for the geometric optics model. . . . . 42

- 7 Comparison of measured first and second harmonic coefficients with 2-scale and geometric optics models at 37 GHz. JPL's WINDRAD data were measured at a wind speed of 9 m/s at 5 m elevation, which is very close to the wind speed of 10 m/s at 19.5 m elevation for the measurements by Etkin et al. [11] and Dzura et al. [13].  $k_d = 230$  1/m and  $T_s = 12^\circ$  C. Cox and Munk's slope distribution is used for the geometric optics model. . . . . , 43
- 8 A simple model to illustrate the effects of hydrodynamic modulation. Two tilted facets with slopes  $= \pm S$ . Facet A is flat, while facet B is modulated by small scale roughness. . . . . 43
- 9 The second harmonic coefficients of theoretical Stokes parameters as a function of incidence angle. The Stokes parameters of emission from small scale waves without the large scale tilting evaluated using the SPM and that of emission from large scale surfaces without small scale perturbations evaluated using the Geometric Optics model are included to illustrate the relative contributions of small and large scale waves.  $k_d$  is 120 and 230 rad/m for 19.35 GHz and 37 GHz, respectively.  $T_s = 12^\circ$  C. . . . . 44
- 10 Comparison of the polarimetric Stokes vectors versus the azimuth angle  $\phi$  calculated by using Monte Carlo simulation and the SPM for one-dimensional periodic random rough surfaces with  $\sigma = \lambda/15$  (or  $k_0\sigma = 0.419$ ) at  $\theta = 40^\circ$  incidence. The sea water dielectric constant is  $28 + i36$ , and a surface temperature of  $T_0 = 300$  Kelvin is assumed. . . . . 45
- 11 Comparison of the polarimetric Stokes vectors versus the azimuth angle  $\phi$  calculated by using Monte Carlo simulation and the SPM for one-dimensional periodic random rough surfaces with  $\sigma = \lambda/15$  (or  $k_0\sigma = 0.419$ ) at  $\theta = 70^\circ$  incidence. The sea water dielectric constant is  $28 + i36$ , and a surface temperature of  $T_0 = 300$  Kelvin is assumed. . . . . 46

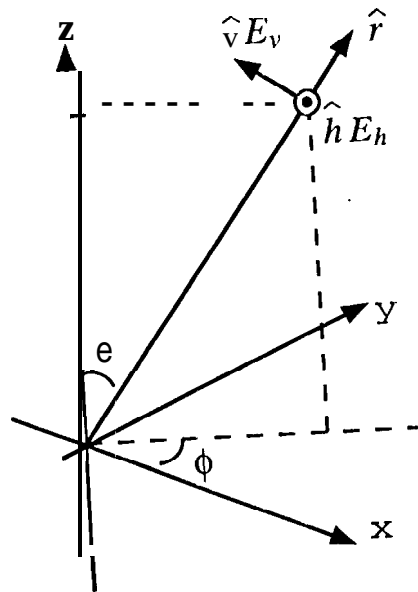
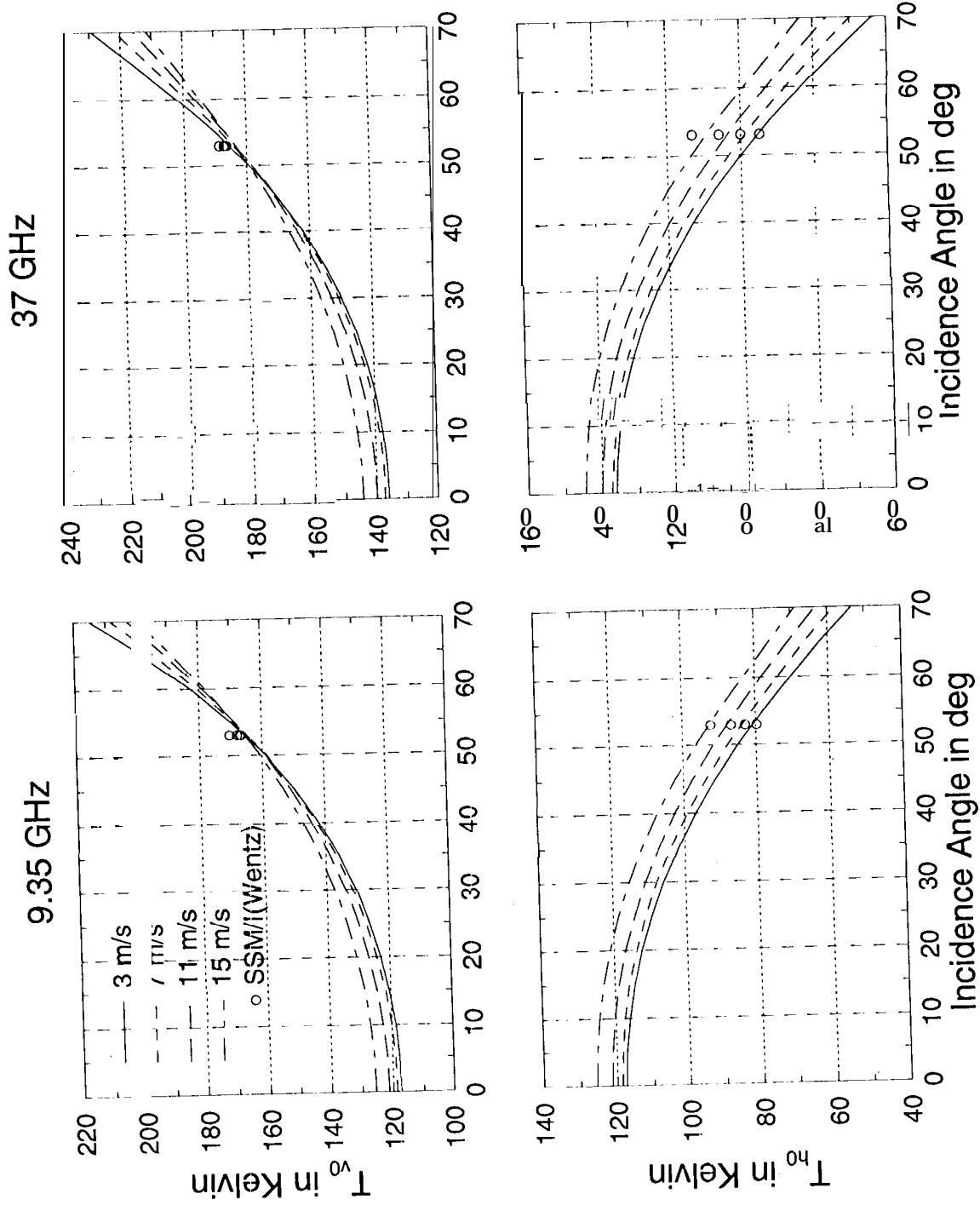


Figure 1





# JPL WINDRAD 93 DATA VS. THEORY

Wind=11 m/s@5m;  $\theta=30$  deg

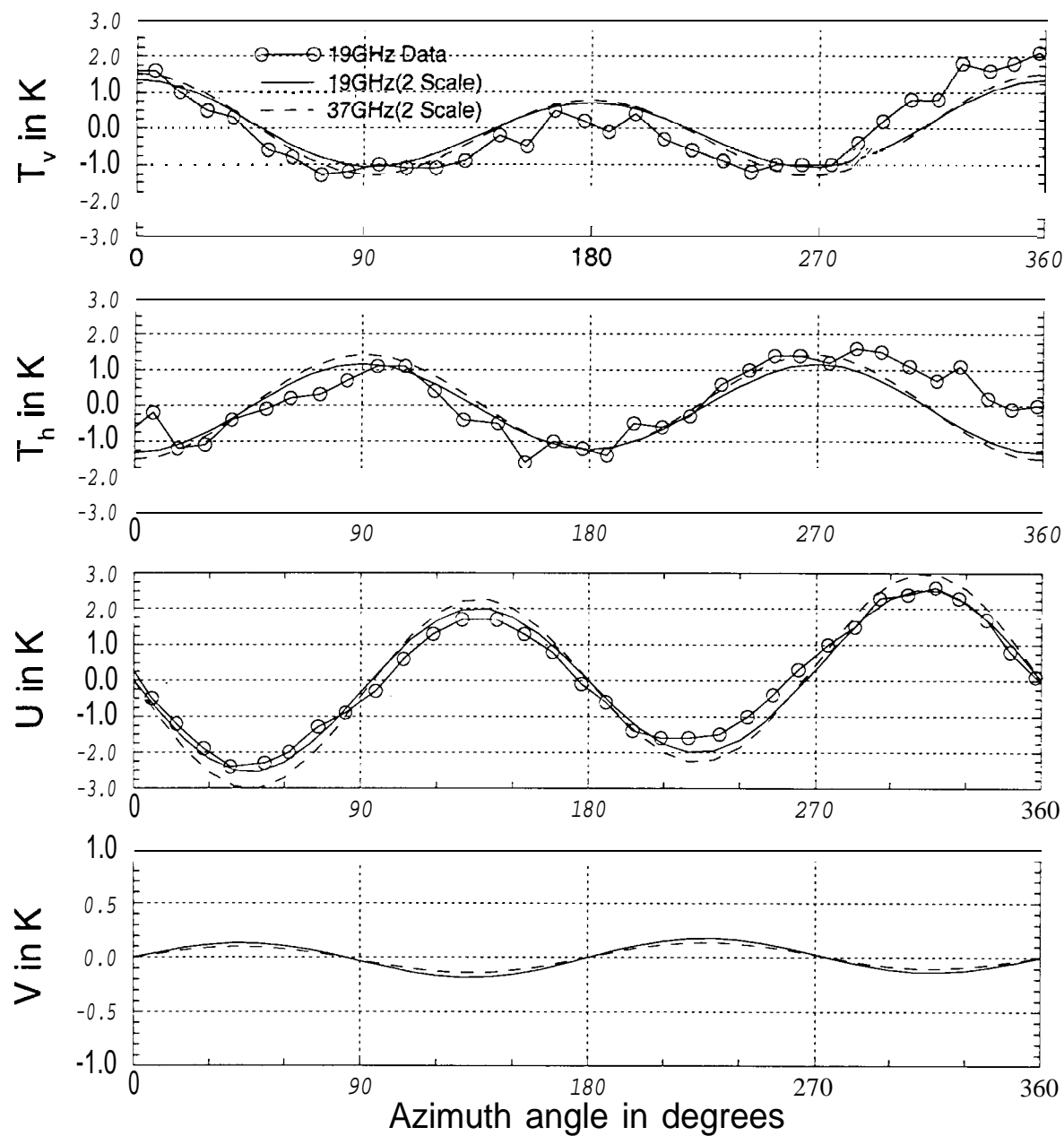


Fig 3

# JPL WINDRAD'94 DATA VS. THEORY

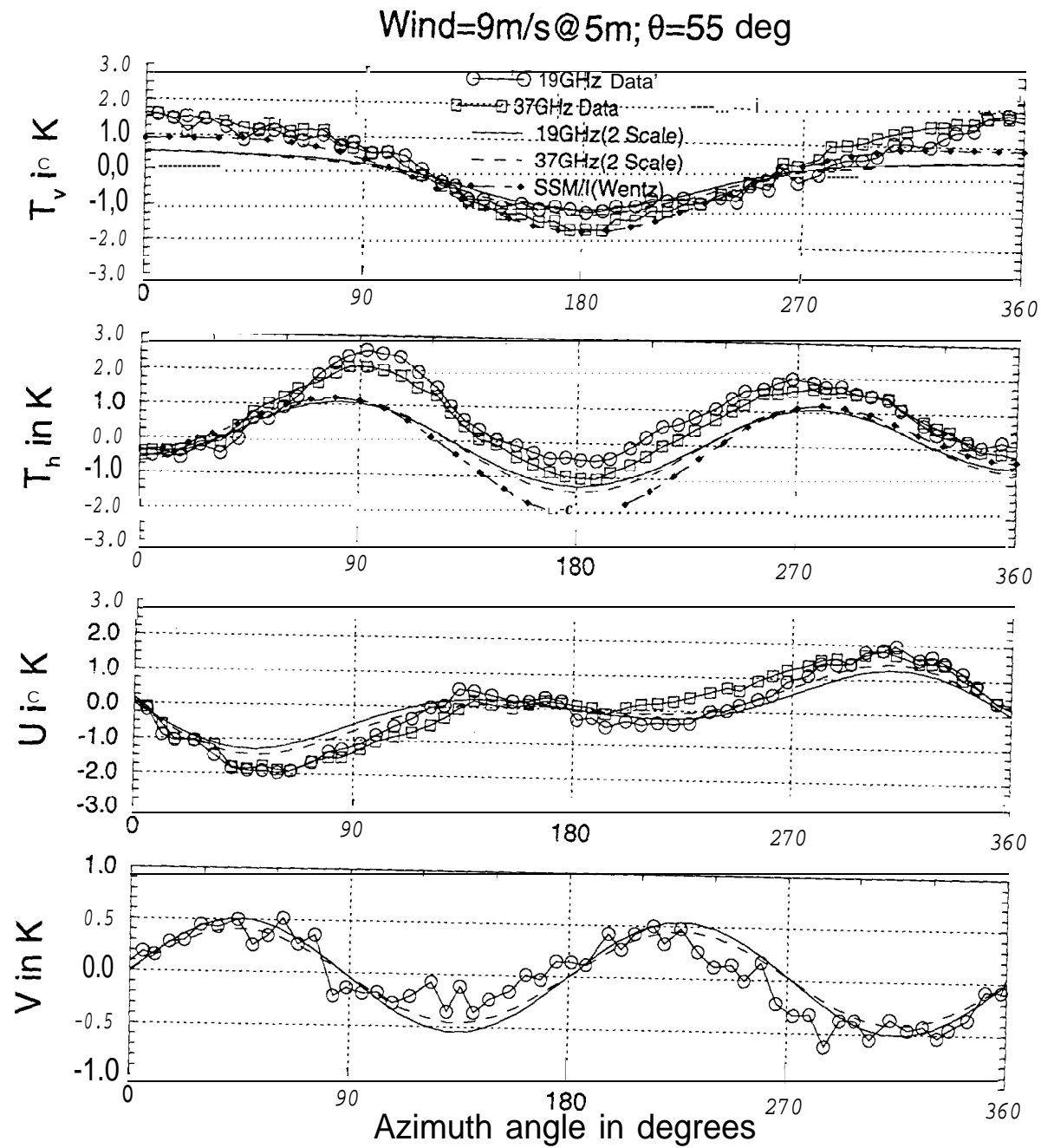
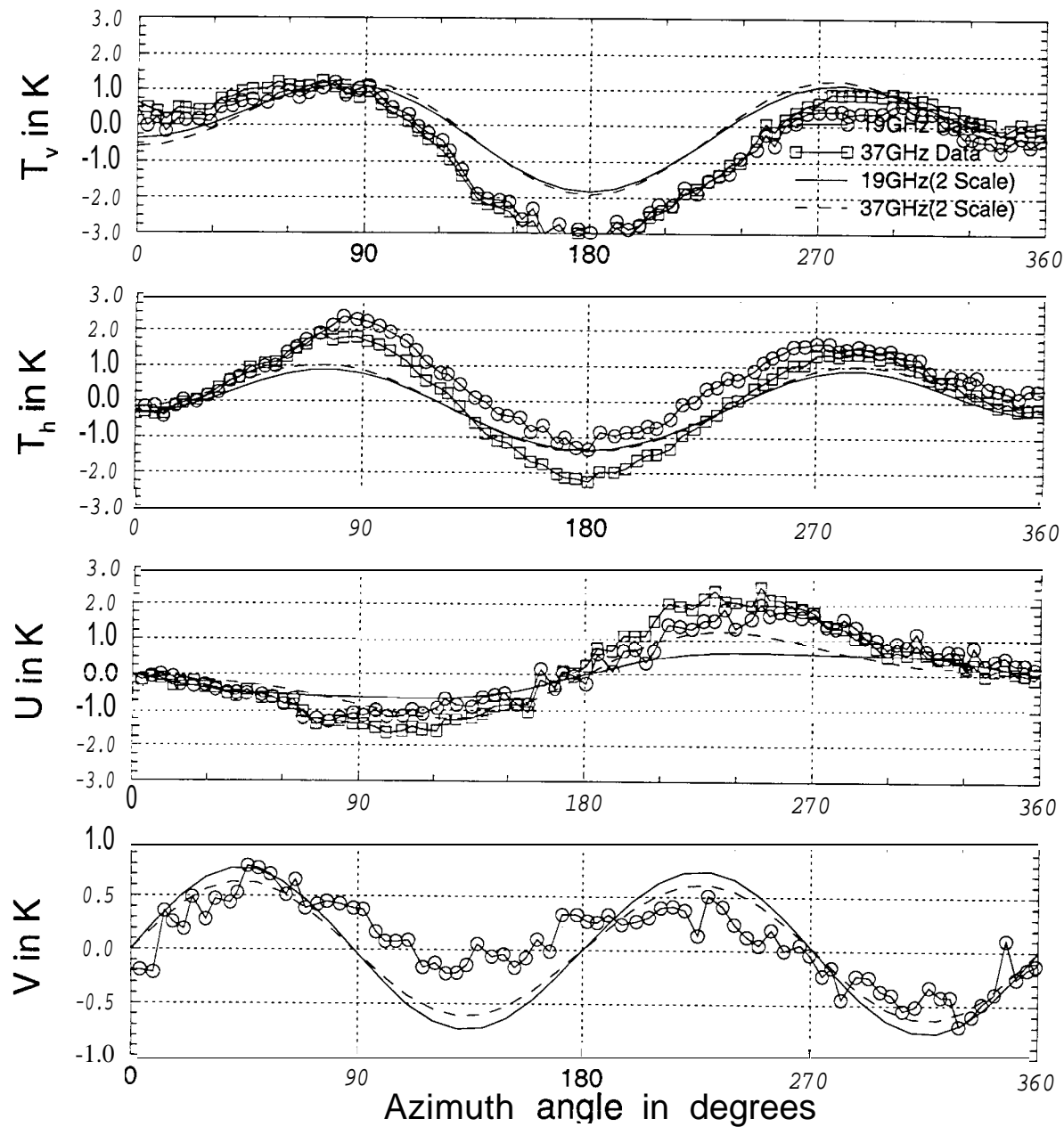


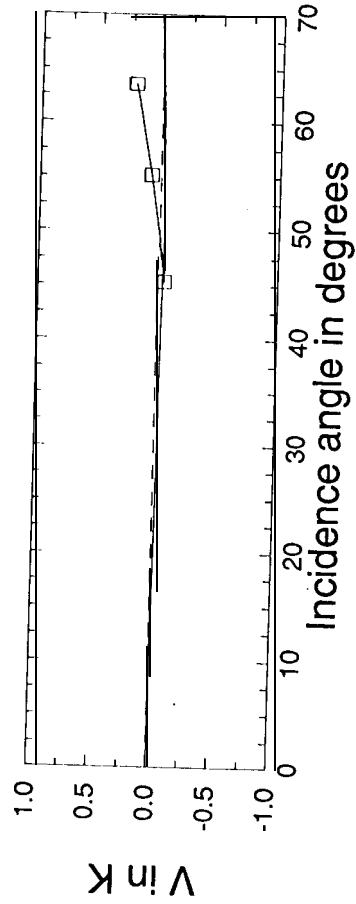
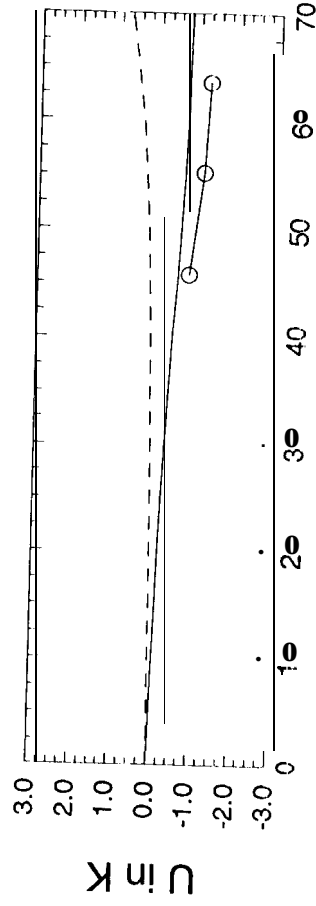
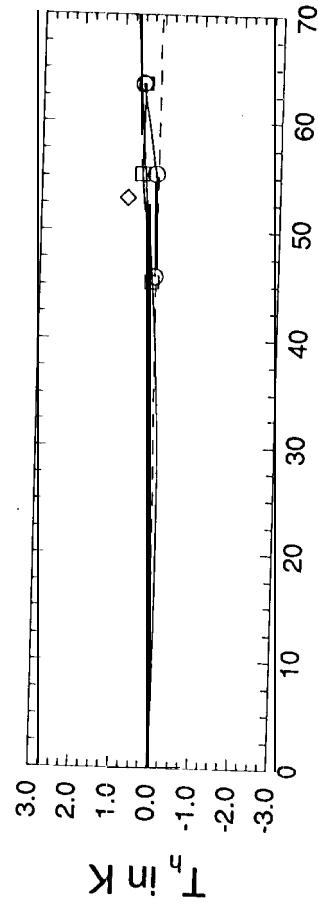
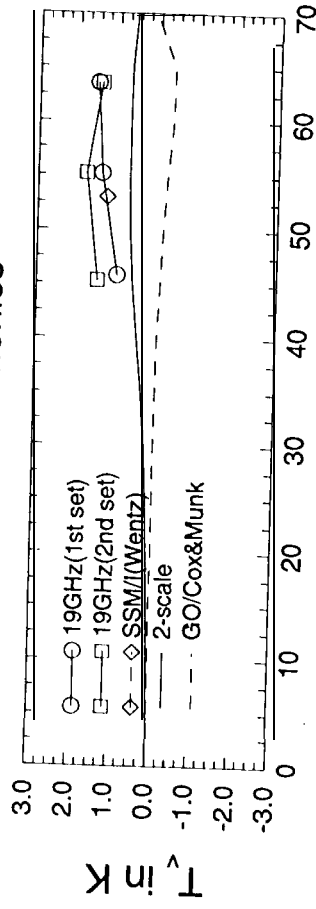
Fig 4

# JPL WINDRAD'94 DATA VS. THEORY

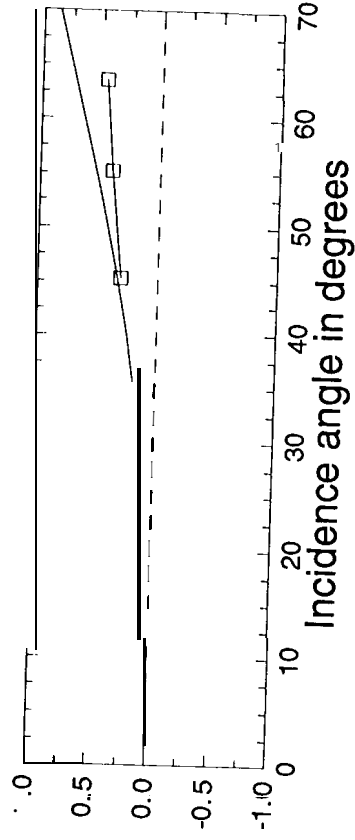
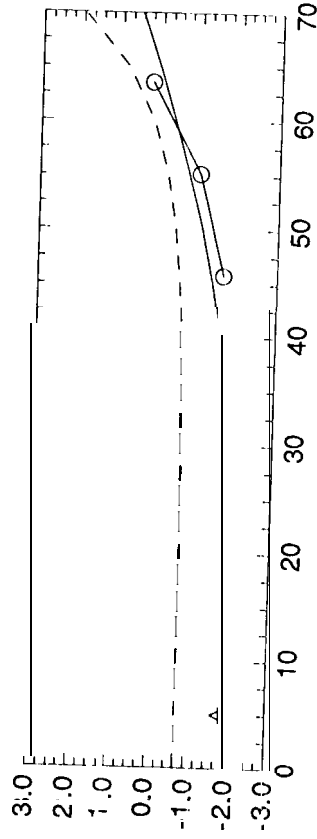
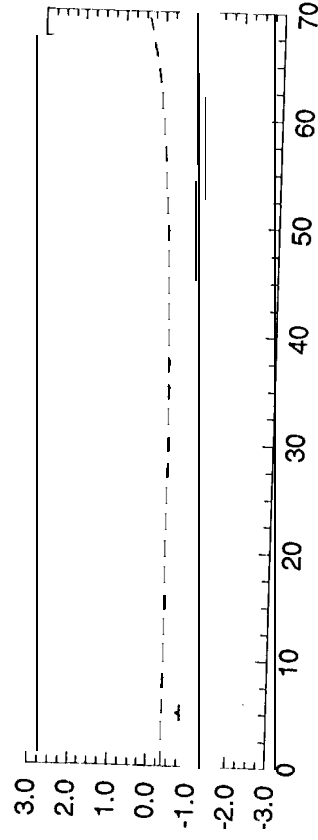
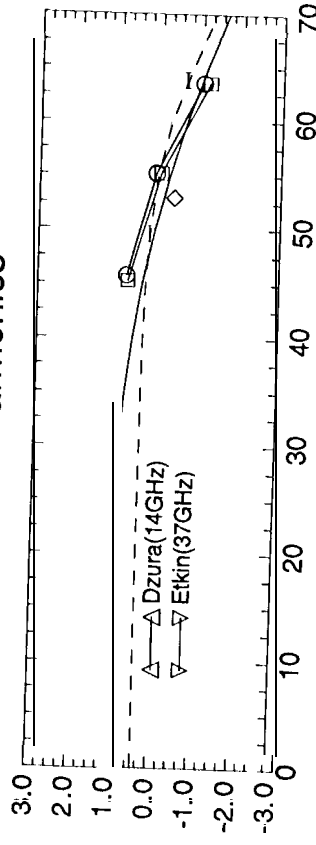
Wind=9m/s@5m;  $\theta=65$  deg



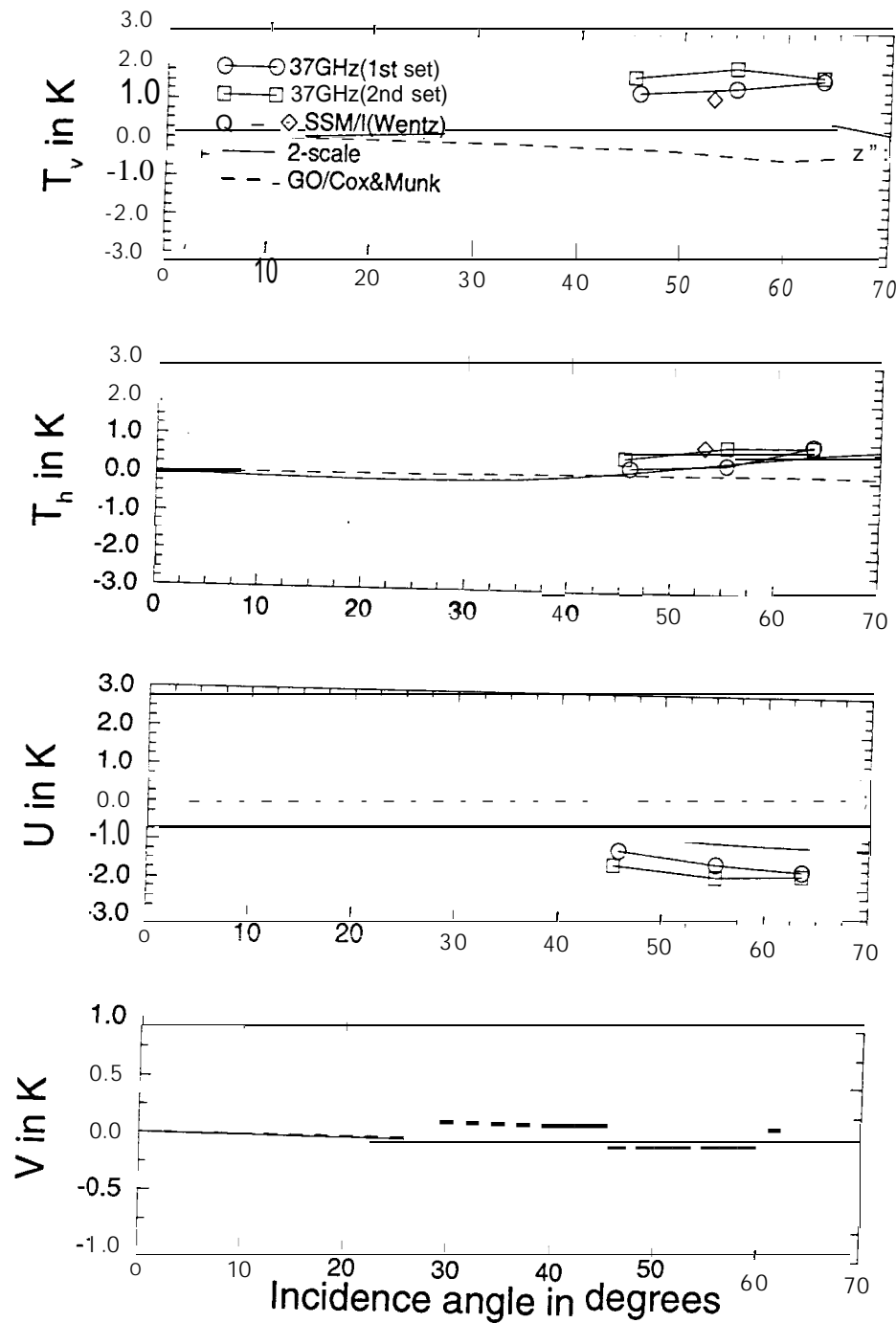
# 1st Harmonics



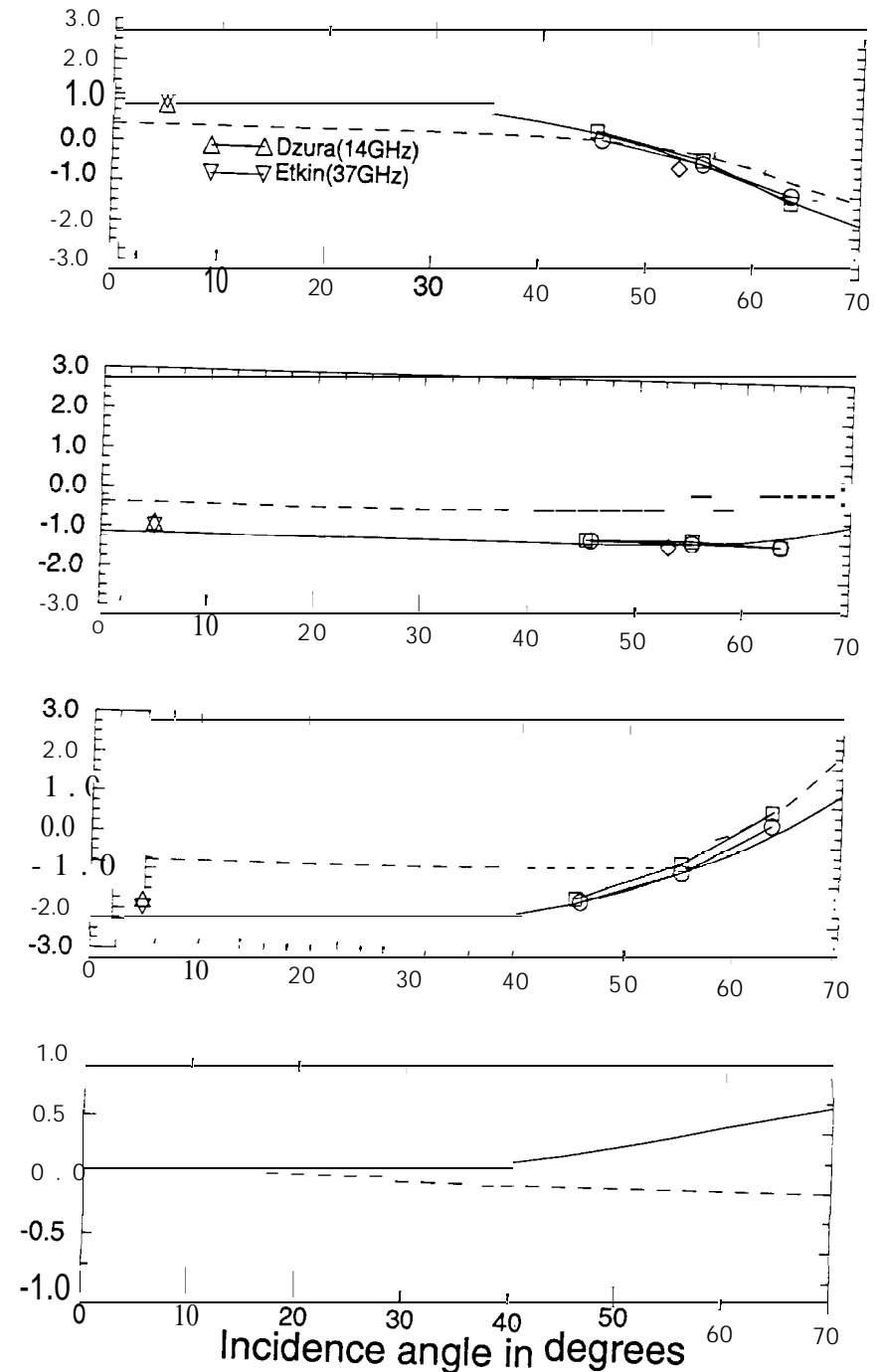
# 2nd Harmonics



# 1st Harmonics



# 2nd Harmonics



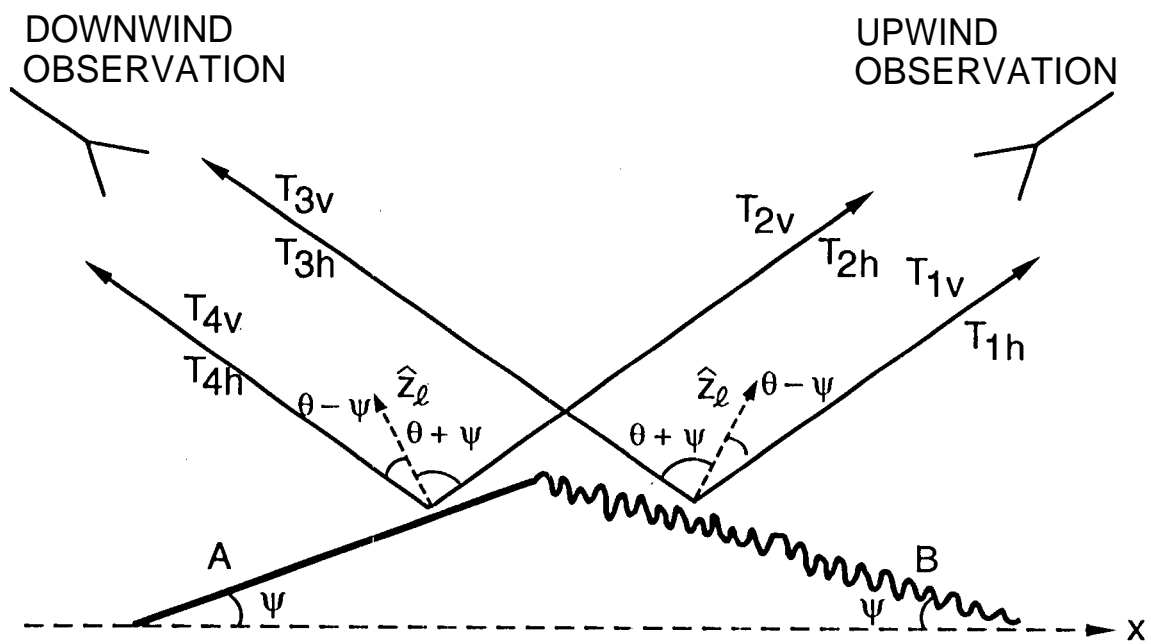
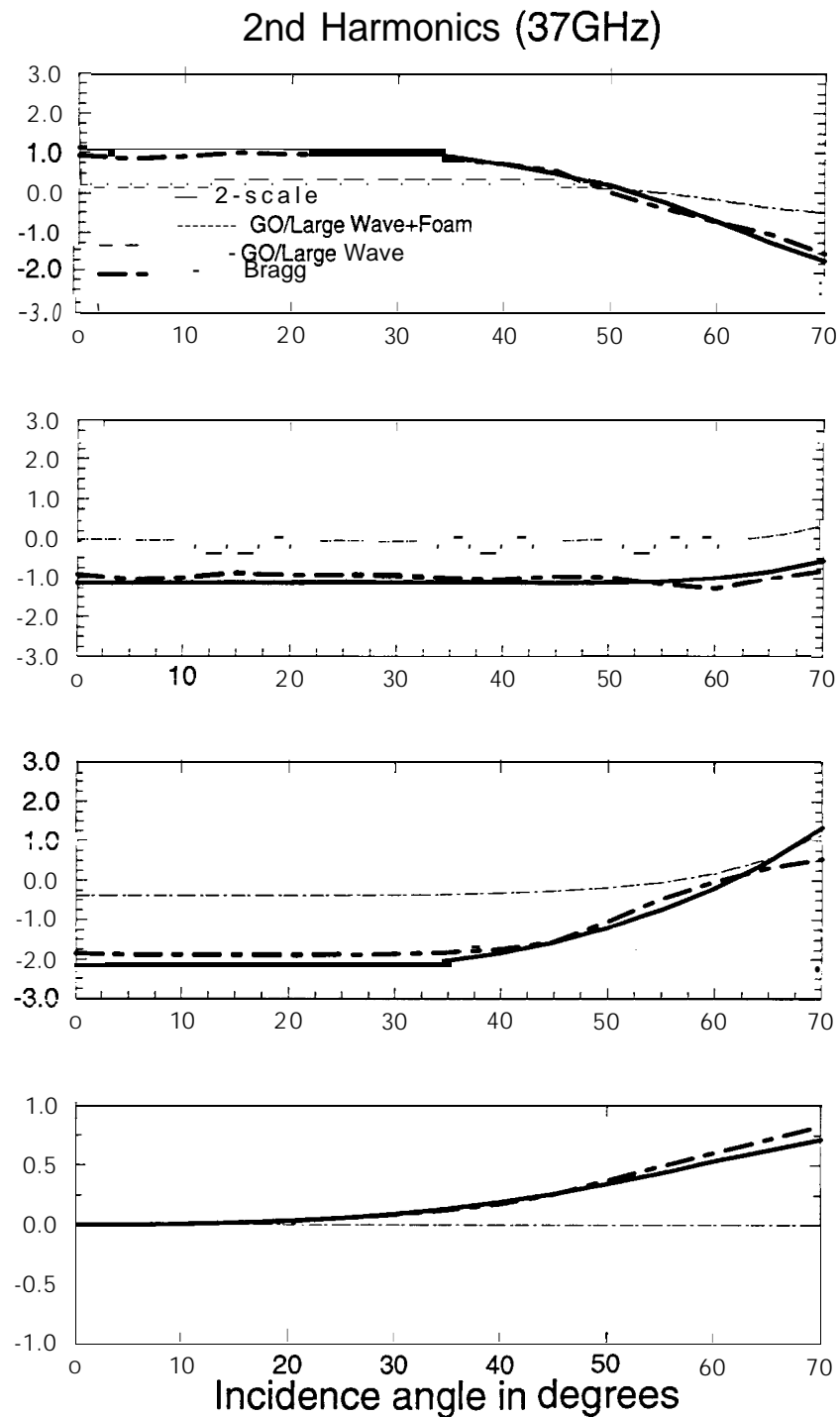
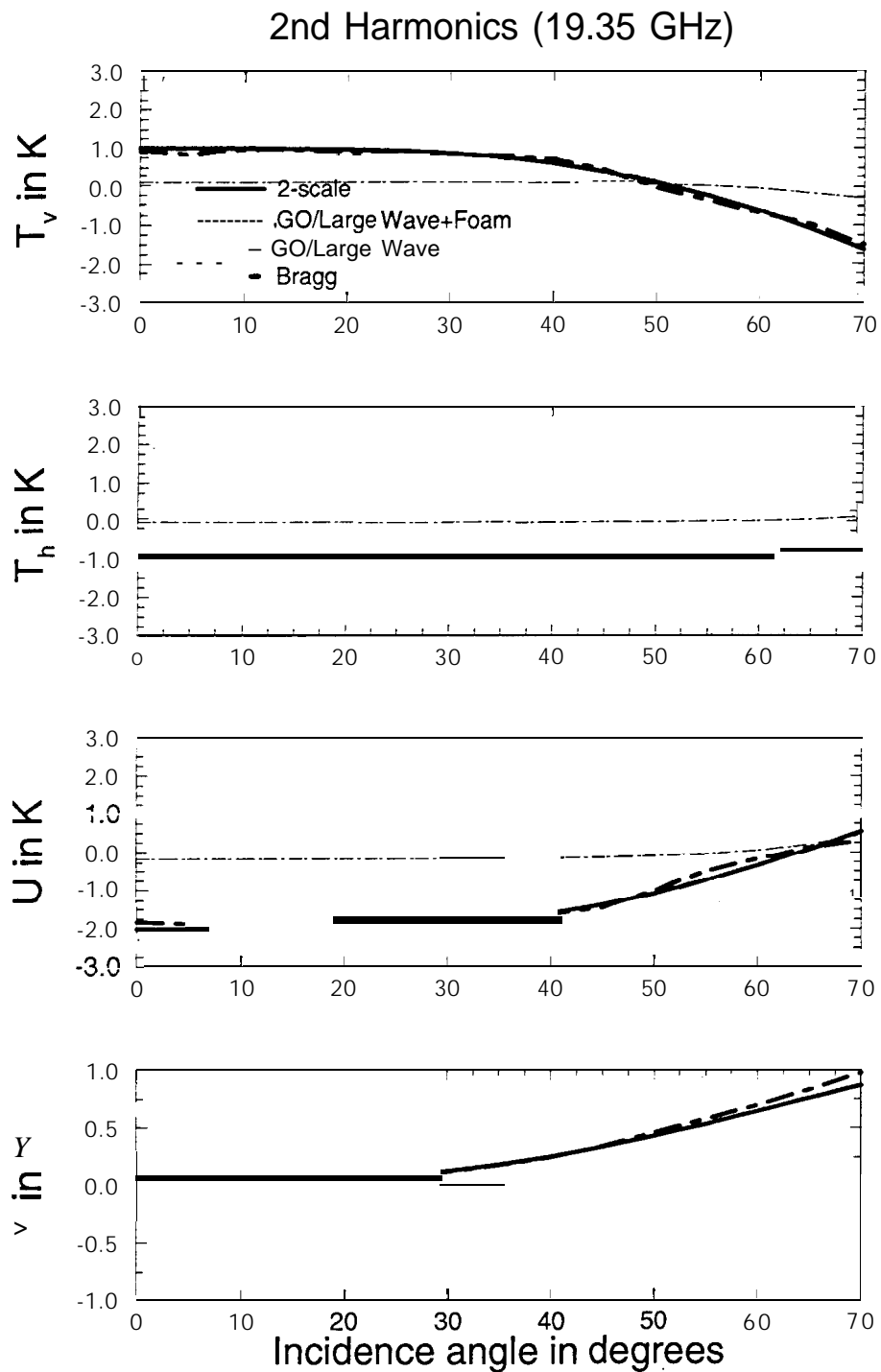
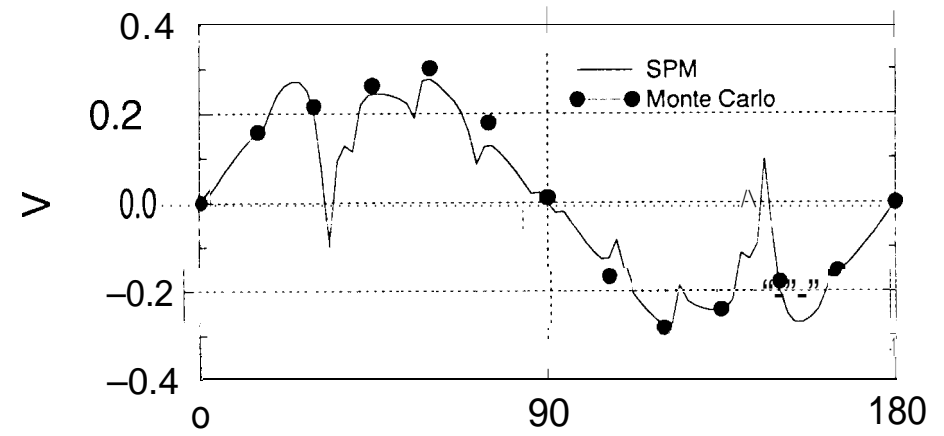
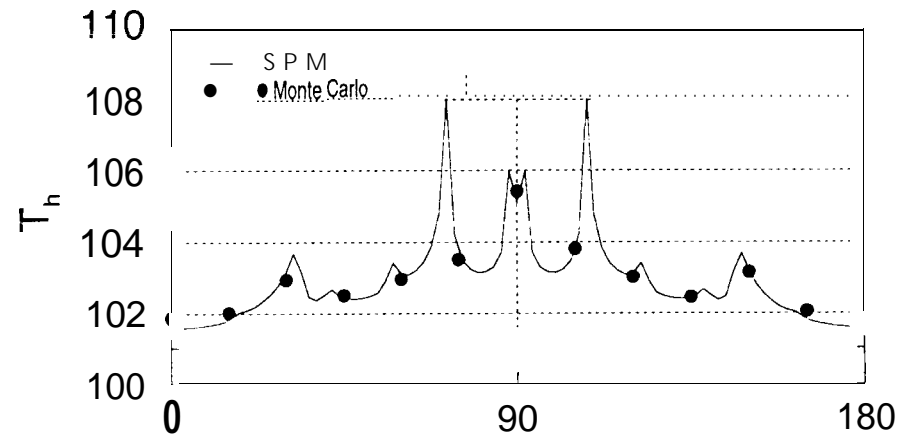
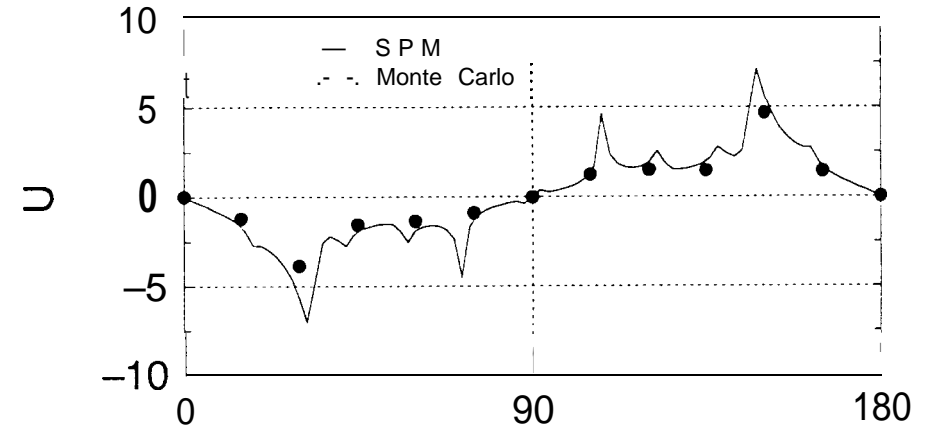
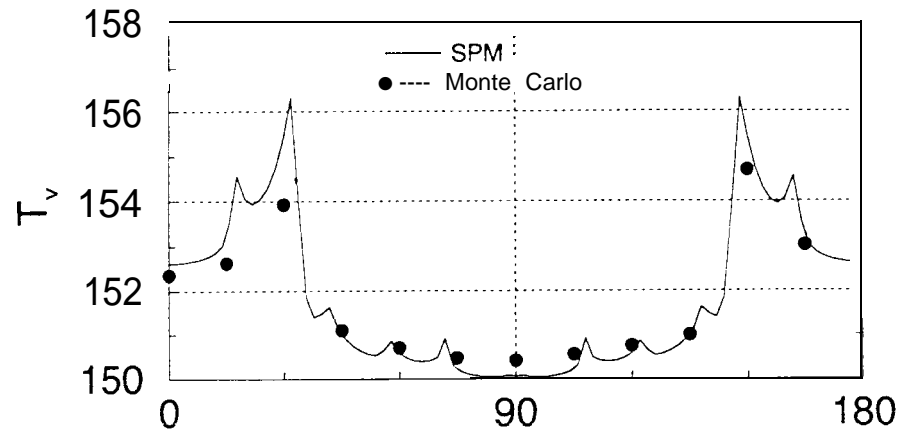


Fig 8





$\theta=40$  degrees



Azimuth angle  $\phi$  in degrees

Azimuth angle  $\phi$  in degrees

$\theta = 70$  degrees

